Design of Control Electronics for the Ram Energy Distribution Detector

Adithya Venkatramanan

Thesis submitted to the faculty of the Virginia Polytechnic Institute and State University in partial fulfillment of the requirements for the degree of

Master of Science
In
Electrical Engineering

Gregory D. Earle, Chair
Kwang J. Koh
Brian Lattimer

August 13, 2015
Blacksburg, VA

Keywords: ram wind sensor, cubesat, instrument electrical design

Design of Control Electronics for the Ram Energy Distribution Detector

Adithya Venkatramanan

ABSTRACT

The bulk motion of the neutral gas at altitudes between about 200 and 600 km is an important factor in predicting the onset of plasma instabilities that are known to distort and/or disrupt high frequency radio communications. A ram wind sensor is a space science instrument that, when mounted on a satellite in low-Earth orbit, makes in-situ measurements of the component of the neutral gas velocity that lies along the orbit track of the satellite. The instrument works by changing the voltage on one of a set of grids and measuring a corresponding electron current generated by ions flowing through the grid stack and detected by the microchannel plate, generating a function of current vs. voltage called an I-V curve. Traditionally, the size and power requirements of ram wind sensors has limited their use to larger satellites. In this thesis, the electrical design and basic testing of a cubesat compatible RWS known as the ram energy distribution detector (REDD) are described.

The mechanical design of the REDD sensor is first described, and the requirements of the electrical design are presented. The electrical requirements are based on both the characteristics of the ionosphereic flight environment, and on the size and power requirements typical of the small cubesat platforms for which the instrument is intended.

The electrical hardware is then described in detail. The microcontroller design is reviewed as well, including the instrument's operating mode, and timing scheme.

Test data showing the basic functionality of the instrument are then presented. Bench tests validate the design by confirming its ability to control voltages and measure small electron currents. End-to-end tests were also performed in a vacuum chamber to mimic the ionospheric environment. These data are presented to show the ability of the REDD sensor to meet or exceed its design specifications.

Acknowledgements

I would like to thank my adviser Dr. Earle for his uncommonly calm attitude and helpful advice throughout this project. I would also like to give special thanks to Lee Kordella and Debbie Collins for all their help.

All photos by author, 2015

Table of Contents

List of Figures

List of Tables

Chapter 1-History and Functionality of REDD

In the past, the US Air Force launched the communication/navigation outage forecast system (C/NOFS) satellite, which was designed to measure various geophysical variables associated with the initiation of equatorial spread F (ESF) irregularities in the ionosphere[1-3]. The non-laminar perturbations in the ionospheric plasma density caused by the ESF instability produce reflection, refraction and scintillation of electromagnetic signals propagating in the medium. This process affects both the military and civilian systems since it perturbs electromagnetic signals over a wide range of frequencies. Despite the availability of abundant statistical data regarding the onset, intensity and duration of ESF events, it is difficult to accurately predict its occurrence. The goal of the C/NOFS mission is to demonstrate that such prediction is feasible, by linking pseudo real-time data with state of the art geophysical models.

The C/NOFS satellite was launched into a low inclination elliptical orbit with a perigee near 400 km. The satellite carried a wide variety of instruments to study the properties of the ionized and neutral gases, as well as the electric and magnetic fields pervading the medium. Most of these instruments have abundant flight heritage except the neutral wind meter, which was a new instrument that was never flown before. This instrument was of significant importance since the bulk flow of the neutral gas is a key parameter in the onset of ESF.

The C/NOFS neutral wind meter comprises two neutral wind sensors developed at the University of Texas at Dallas. One of these sensors is designed to measure the two components of the neutral wind in the plane perpendicular to the satellite's velocity vector. The arrival angle of the neutral gas relative to the satellite's velocity vector was estimated by the device[4] based on a differential pressure measurement. The component of the neutral flow along the orbit track was measured by a device called the ram wind sensor (RWS) [5].

The possibility of flying large research satellites have been inhibited by the limited budgets available for spaceflight experiments. In response to this, the space science community has begun to embrace the idea of flying smaller, cheaper satellite systems. These are characterized as microsats (total mass less than 100 kg), nanosats (mass less than 10 kg), and picosats (mass less than 1 kg). CubeSats[6] are typically in the nanosat class. These scientifically useful systems involve satellites that have standardized architectures and straightforward specifications to minimize cost and complexity. Both NASA and the NSF have encouraged the space science community to use CubeSats for both scientific and educational purposes by introducing funded programs for the same. There have been many CubeSat launches so far, but no CubeSat mission has yet flown an RWS. This is because the size, weight, power requirements for well-established RWS designs are incompatible with the CubeSat platform. Keeping this in mind, our research group is trying to develop a miniaturized CubeSat version of the RWS, called the ram energy distribution detector (REDD). The initial goal is to show laboratory data from a series of tests conducted in a vacuum chamber to validate its feasibility for in-flight measurements. For this thesis, I have designed and tested the electronic system that controls this REDD sensor.

The Ram Energy Distribution Detector

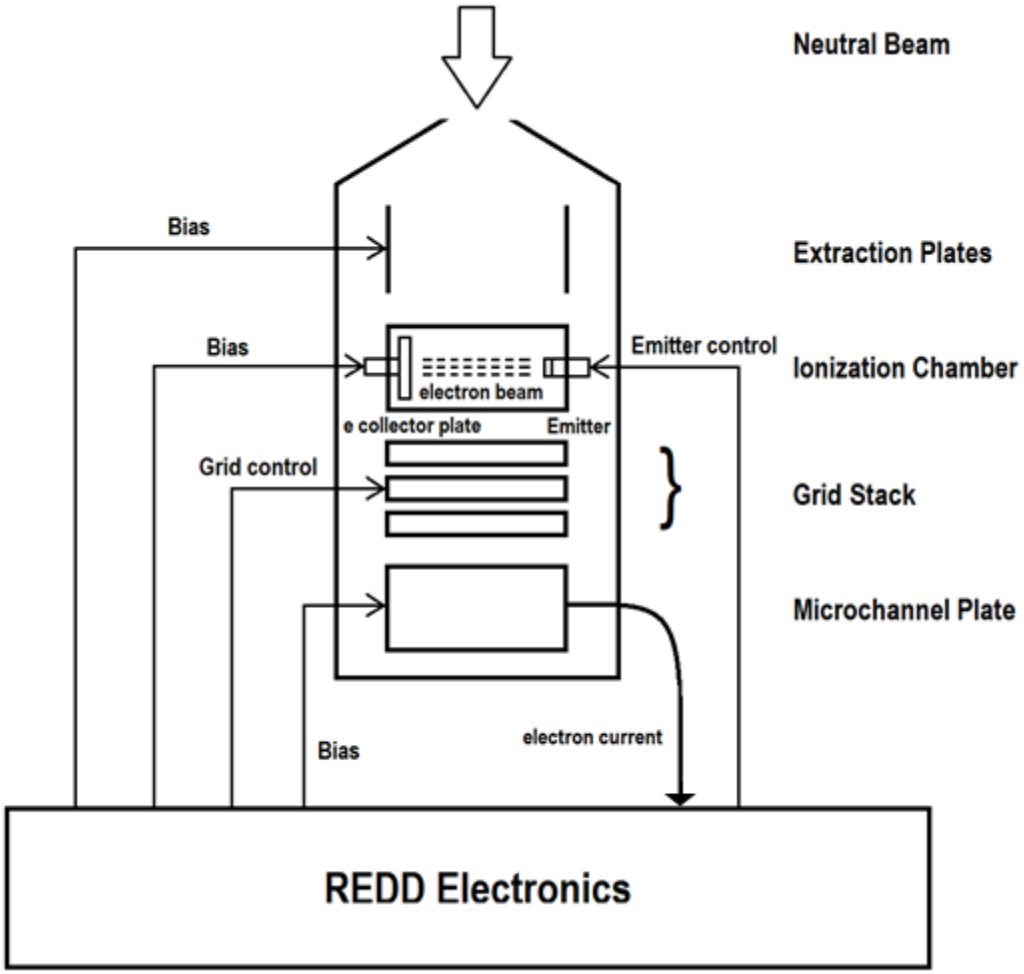

Figure 1: Overall system block diagram for the CubeSat compatible REDD sensor.

A basic high-level diagram of the REDD sensor is shown in Figure 1. At the altitudes of interest, the beam of particles that enter the aperture will be comprised of neutral particles, positively charged ions, and electrons, with the latter two being minor constituents, constituting about 1% of the total flux. However, to accurately analyze the neutral beam, it is necessary to remove the ions and electrons from the incoming stream. This is accomplished by placing electrically biased extraction plates inside the REDD instrument near the aperture. As the gas flows past these plates, the charged particles are removed from the beam without significantly affecting the neutral particle distribution.

The supersonic beam of neutral particles next enters the ionization chamber where it intersects a beam of electrons that is produced by an emitter and absorbed by an electron collector plate housed within the ionization chamber. So as to measure the energy distribution of the neutral particles electronically, a small fraction (about 1 in 10^6) of the particles are ionized using the electron beam. The momentum of the electrons in the ionizing beam is negligible compared to that of the incoming neutrals, most of which have a mass close to 16 amu at ionospheric altitudes. As

a result, the thermal distribution of the ions produced in the beam is essentially the same as that of the incoming neutral beam. After passing through the grid stack, the ions are detected using a microchannel plate (MCP).

The grid stack comprises three flat, electrically conductive grids in a stacked parallel-plane configuration, where the normal to the grids is aligned in the ram direction. Two of these grids, namely the aperture (outermost) grid and suppressor grid are held at constant potentials (typically spacecraft ground), while one grid is driven by a positively-swept periodic voltage signal. The grid with the swept voltage signal is called the retarding voltage (RV) grid and it sets up a time-varying energy barrier to the incoming ions.

Ions collected by the MCP are amplified and converted into an electron current (through the MCP gain), which acts as the input to the REDD electronics. In addition, the third grid can be held at negative potential to prevent the electrons from escaping from the MCP when it is hit by incoming fast-moving ions. The first grid called the aperture grid, sits between the ionization chamber and the retarding grid, which is typically held at ground, but can also be set to a negative potential to pull the ions generated in the ionization chamber into the grid stack during laboratory testing. The purpose of the REDD electronics is to sweep the voltage on the RV grid, control the voltages on the suppressor and aperture grids, control the emitter in the ionization chamber, provide bias voltages for the MCP and measure the detector current.

When the RV grid voltage is at ground all of the incoming ions will pass through it, hit the MCP and generate an electron current. But as the RV grid voltage is swept to increasingly positive values, fewer of the incident ions have sufficient energy to pass through, so the MCP electron current is reduced. Hence the raw data signal is obtained by measuring the MCP output electron current, which is proportional to the number of ions incident on the MCP as a function of the voltage applied to the RV grid. The resulting current-voltage (*IV*) characteristic can be analyzed using the retarding potential analysis technique[7-8] to measure the ram component of the velocity of the incident neutral beam relative to the spacecraft.

The *IV* characteristics are analyzed using a Levenberg-Marquardt[9] nonlinear fitting routine to solve for the velocity of the incident neutral beam. The form of the function used in these fits is given by Knudsen[8] as

$$N = \sum_i f_i \left[\frac{1}{2} + \frac{1}{2}\mathrm{erf}(k_i) + \frac{exp(-{k_i}^2)}{2\sqrt{\pi}a_i}\right], \quad (1)$$

$$k_i = \frac{vcos\theta}{\sqrt{2KT_i/M_i}} - \sqrt{\frac{eV}{KT_i}}, \quad (2)$$

$$a_i = \frac{vcos\theta}{\alpha_i}, \quad (3)$$

where the sum is carried out over the number of species comprising the ambient gas, f_i is the fractional composition of each component gas, V is the retarding potential, and θ is the angle between the incoming beam and the aperture plane. The other parameters in Eqs. (1) - (3) are : N, the ion density; v, the velocity of the beam; M and T, the mass and temperature of the ionized

constituents; α_i, the ion thermal speed, and Boltzmann's constant K. The total current is then given by

$$I = \eta N e v A \,, \tag{4}$$

where η is the grid transparency factor, e is the fundamental unit of electronic charge and A is the collecting area. Through a nonlinear fit to the *IV* curve, the ion concentration, temperature, and relative speed of the ions in the spacecraft frame can be inferred. Idealized retarding potential analysis *IV* curves for a flowing gas with constant temperature (top) and constant velocity (bottom) are shown in Figure 2.

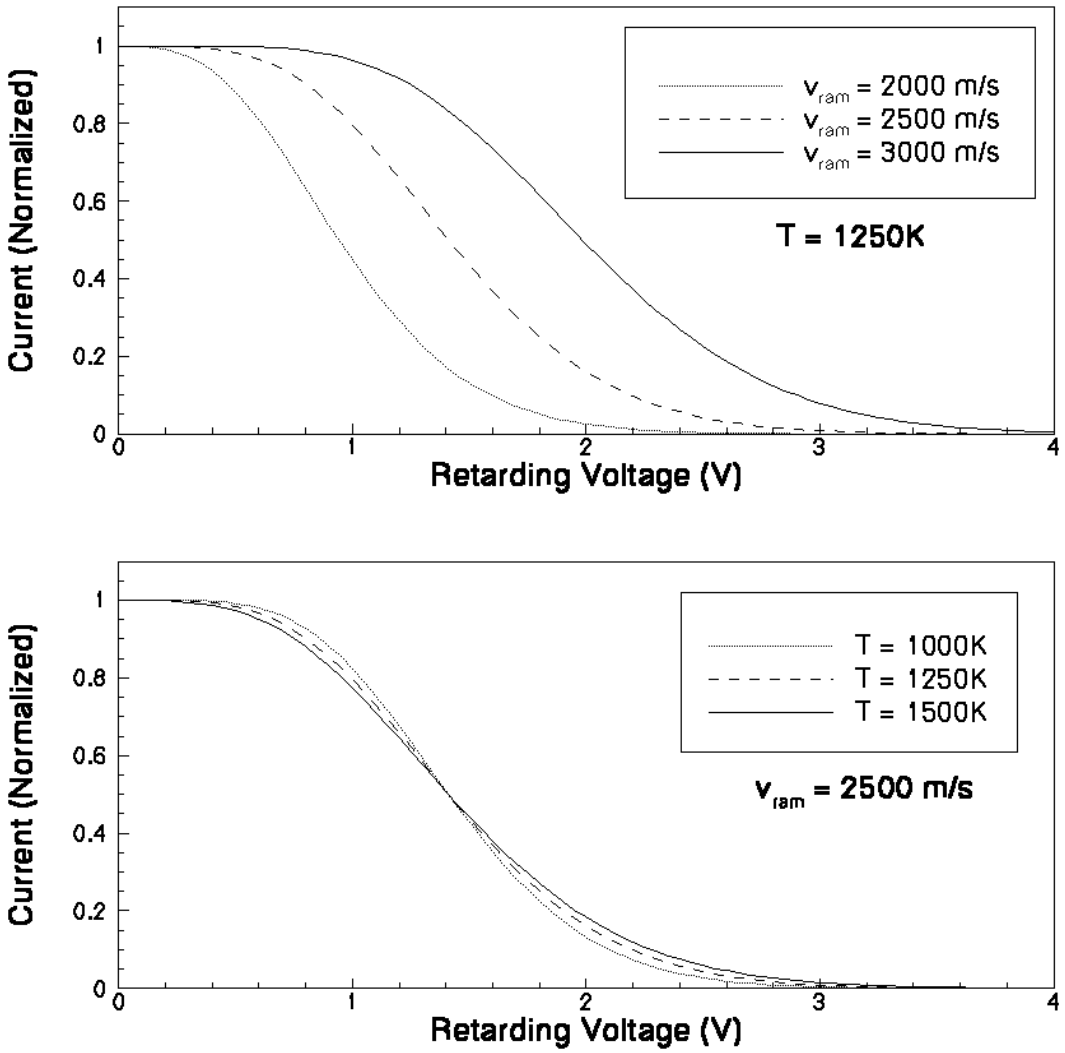

Figure 2: Curves showing the results of Eqs. (1) - (4) to calculate the current for a beam comprised of pure argon as the velocity and temperature vary. All of the plotted curves have been normalized.

Chapter 2 – REDD Design Requirements

The basic requirements of the REDD electronics are to control the voltage of the grids within the instrument, to measure the electron current coming out of the MCP detector corresponding to each voltage on the retarding grid, to control the emission in the ionization chamber, to provide bias voltages for the MCP and extraction plates, and to report the data back for monitoring purposes. The mechanical REDD design dictates how many grids the REDD electronics must control. The REDD sensor must be able to set the grid voltages to some specific degree of accuracy, and it must accurately measure the MCP electron current with some required precision. In addition, it is desired that the REDD sensor be able to change the characteristics of its retarding voltage sweeps, so that its performance can be optimized for particular geophysical conditions. There must also be some method of communication between the external world and the REDD instrument in order to log the IV curve measurements.

Mechanical Design

A CAD model of the CubeSat RWS (REDD) sensor mechanical assembly is shown in Figure 3. The central cylindrical region surrounded by the cross-track sensor chambers is the REDD instrument. Just beneath the aperture of the instrument sits the ionization chamber that houses the emitter and an electron collector plate. It ionizes a small fraction of the incoming neutral particles so that their energy distribution can be measured electronically. Below the ionization chamber is the grid stack comprising three flat, electrically conductive grids in a stacked parallel-plane configuration. The outermost aperture grid, through which the ions first pass, is held at ground potential. This ensures that the ion trajectories are not perturbed by the electric fields in the instrument. The second grid is the retarding grid, whose voltage must be swept to generate the IV curve that comprises a measurement set. The third grid can be biased to a negative potential to prevent electrons from moving across the grid in either direction, or it can be held at ground to isolate the MCP from the retarding grid. In practice we will try both approaches once the REDD sensor is integrated for vacuum testing. The MCP detector is at the back of the REDD instrument. It collects these ions and produces a proportional electron current which we need to measure to generate the IV curve for each measurement set.

Mechanical and Electrical Requirements

In order to be compatible with the CubeSat platform, the mass of the REDD instrument (including the sensor structure and electronics) is ≤ 4.5 kg, and the entire mechanical portion of the instrument is contained within an 8.5 x 8.5 x 4.5 cm volume. The design has been approached to enable easy and quick assembly of the sensor structure, including grid rotation and stack-up. After being aligned and fastened, the grids, extraction plates, MCP, and the ionization chamber are connected to the REDD electronics via soldered lead wires.

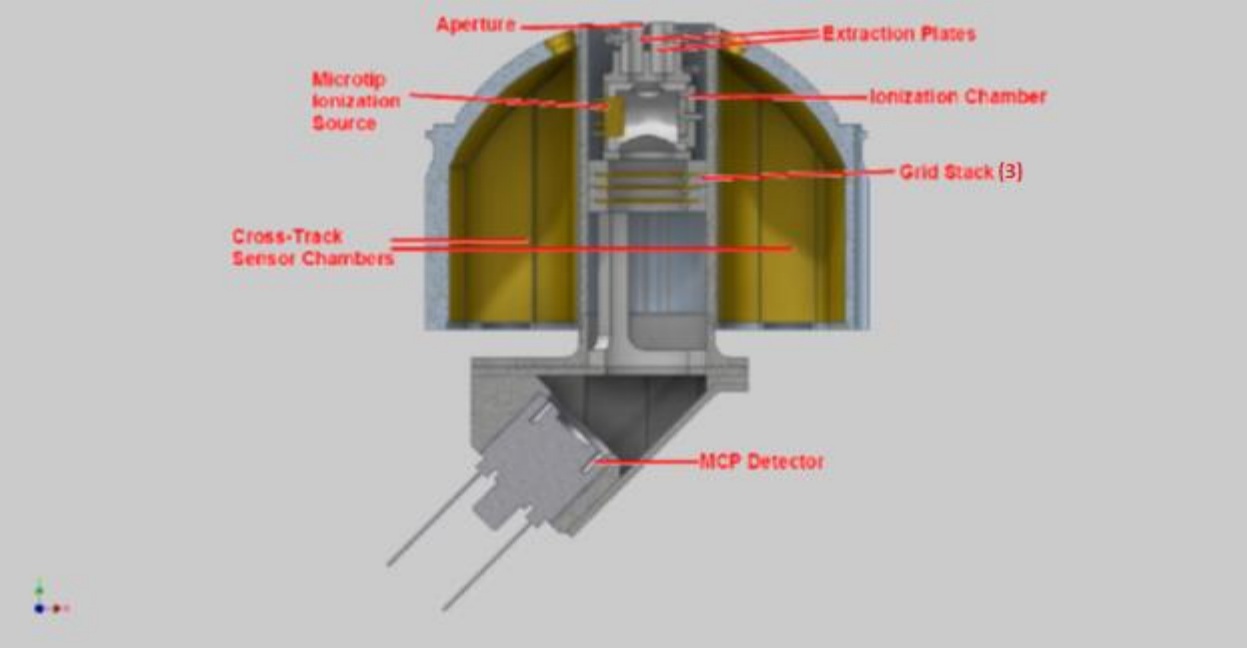

Figure 3: Full cross sectional front view of the ram energy distribution detector.

The specific requirements of the REDD electrical system, such as the range of currents that must be measured, the range of voltages that must be set on the grids, and the RV sweep rate, come from a combination of the properties of the ionosphere, and from experience with measurements on previous missions. The requirements are summarized in Table 1. Though the actual electron current range in-flight from the microchannel plate depends on several factors such as the gain of the MCP, size of the aperture, efficiency of the ionization process, solar conditions, orbit altitude, instabilities in the ionosphere, etc., an intuitive first cut estimate can be derived based on the density of ions in the ionosphere and their speed relative to the spacecraft. The relation is given in equation 4. Taking into account the typical range of ion densities, speed of the satellite and drift velocities of the ions in the region where the REDD instrument will be flying, and the aperture area and transmission coefficient of the grid stack, gives a dynamic range of the signal level between 10 μA on the high end and 100 pA on the low end.

In a typical I-V curve (e.g., figure 2) the current approaches zero as the retarding voltage increases. In flight conditions the retarding grid must sweep up to 12 V to produce a complete I-V curve. The suppressor grid may require a large enough negative voltage to prevent electrons from passing through; a sufficient value to repel the electrons is -5 V, so the electronics must be able to drive the suppressor grid at or below this level. The retarding grid sweep must occur in 1 second and include 128 different current-voltage points along the I-V curve. The REDD electronics must therefore be able to set the RV grid bias to at least 128 different voltages within a 1-second period while measuring the corresponding MCP current. Typical temperature values on satellites range from 5° to 30° C, so the REDD electronics must be able to operate in this range, and to survive fluctuations over a somewhat larger range.

Parameter	Value
Measured Current Range	100 pA to 10 μA
Measured Current Accuracy	Greater of 100 pA or 2.5 %
Samples per I-V Curve	64 or 128 (programmable)
I-V Curve Sweep Time	1 s
Retarding Voltage Range	0 V to 12 V
Suppressor Bias	-5 V or Less
Aperture Bias	0 V or Less
Survival Temperature	-20° to 75° C

Table 1: Science-based requirements of the REDD instrument

The requirement for sweep flexibility adds much more complicated constraints to the REDD electrical design. Rather than taking one sample per I-V point, it is desired that several current samples be accumulated and averaged for better accuracy. While every sweep must have a minimum of 128 samples per I-V curve, it is desired that the number of points per sweep might be able to change in-flight. More points in a sweep leaves less time to oversample current points, so there is a trade-off between the oversampling of the current samples and the number of points per sweep. The REDD electronic design should allow the sampling rate and number of points per sweep to be software controlled, to allow different scenarios to be tested.

The voltages on the grids will ideally have flexibility as well. In an environment where the MCP detector current approaches zero at a retarding grid voltage of 4 V, it is useless for half of the voltages in the sweep to be higher than 4 V, so it is desired that the voltage values be able to change in-flight. Furthermore, multiple schemes for changing the voltages are required in the REDD design. In addition to changing linearly with a constant step size, it is desired to have a mode where the retarding voltage stays the same for an entire sweep, which allows for higher spatial resolution in the ion density measurements. Also, as shown in Figure 2, the current changes more rapidly in the middle of the I-V curve and is relatively flat at the two ends. So it is desired to have a mode where the retarding voltage points increase nonlinearly such that they are concentrated in the middle of the voltage range, yielding more points in the middle of the I-V curve than at the ends. This results in better curve-fits during data analysis, and therefore more accurate temperature and velocity data.

Based on these system constraints, an electrical design has been developed to control the grids, sample the detector current, and report the data back for archiving the measurement sets. In the next chapter this electrical design is discussed in detail.

Chapter 3-Analog Electrical Design

A functional block diagram of the REDD electronics is shown in Figure 4. Detailed electrical schematics are shown in Appendix A. The main components of the electrical system controlling the REDD instrument are:

- a linear transimpedance amplifier (TIA) for converting the MCP electron current into a usable voltage, and an analog to digital converter (ADC) for digitizing this voltage;
- a digital to analog converter (DAC) along with gain stages for setting the voltages on the grids;
- a DAC cascaded with a gain stage for controlling the MCP and emitter tips;
- an ADC for measuring the current and voltage on the emitter tips;
- DC to high-voltage DC converters for biasing the MCP and emitters;
- an emitter control circuit;
- and a powerful low cost microcontroller for controlling the converters and communicating with external electronics.

The electrical design is implemented physically using four separate boards: 1) a main board that controls supply generation and power conditioning, signal conditioning, data acquisition, grid bias control, overall system control and data logging; 2) a current measurement board that contains a linear current sensor that interfaces with the MCP detector; 3) a high voltage converter board that is used to bias the MCP; and 4) an emitter control board for controlling the emitter tips. The boards are stacked using mounting screws and physical standoffs, and power and signal measurements are routed between the boards through wire bundles. The survival temperature range of the electronics is designed to be -20° C to 75° C, taking into account the requirement for normal satellite conditions.

The board communicates with external electronics for data logging via a USB (universal serial bus) to TTL (transistor-transistor logic) serial cable. This is chosen because it is easy to interface the UART (universal asynchronous receiver/transmitter) of the microcontroller with any computer's USB port through a terminal program at a configurable baud rate.

The ideology behind breaking the electrical design into four separate boards is to physically isolate the high voltage, low current, power and signal grounds in order to reduce overall system noise, such as spikes caused by capacitive coupling with the digital electronics. It is desirable to reduce leakage current into the current measurement board because the input currents from the MCP detector may be quite small, and any slight interference caused by capacitive coupling or currents leaking through the board substrate could make a measurable difference to the MCP current.

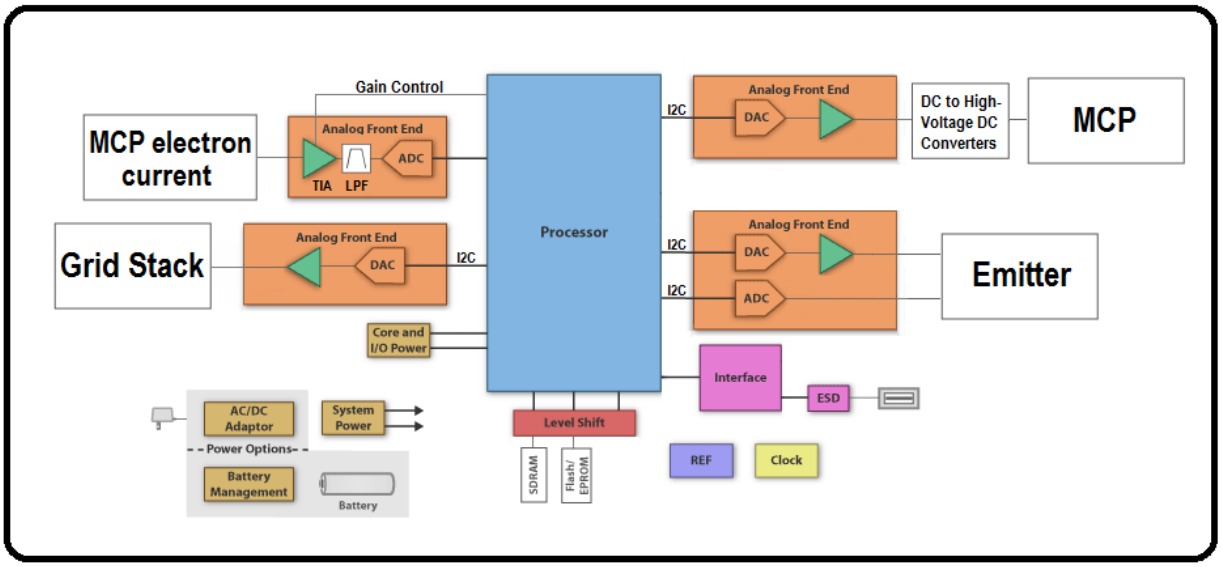

Figure 4: Block diagram of the REDD sensor.

Power Supplies

The REDD instrument receives 12 volts DC from an external power source through a DC barrel jack power connector. From this input the primary power supply of 5 volts is generated as a step-down DC-DC switching power supply that is locally filtered, conditioned, and distributed to the four boards. The supply lines for the analog electronics are derived locally from the main power supplies through a ferrite bead and a bypass capacitor network consisting of low ESR (equivalent series resistance), ESL (equivalent series inductance) capacitors to isolate the power supply switching noise components generated in the digital sections of the circuit. In addition to the main power supplies, supply voltages of ±10 volts and ±2.5 volts are derived from charge-pump voltage converters and step-down DC-DC switching converters. These voltages supply the op-amps in the analog circuitry. The various ADCs and DACs derive their references from voltage reference circuits that generate 1.25 V, 1.5 V, 2.5 V and 3 V.

Grid Control

Figure 5 shows the grid control circuit design. The grid voltages are controlled by a four-channel 16-bit DAC with an output full scale range of 0-3 V, derived from an external reference of 1.5 V with ±0.05% initial accuracy. The DACs have built-in high performance, rail-to-rail output buffers with ultralow crosstalk and are guaranteed monotonic with a maximum INL (integral nonlinearity) error of ±4 LSB (least significant bit) at 16 bits. Each DAC output goes through an amplification stage made up of operational amplifiers with very low input offset voltage, input bias current and output impedance to meet the voltage range requirements on the corresponding grids. The DAC output to the retarding grid goes through a non-inverting stage with a gain of 4, resulting in a retarding grid voltage range of 0-12 V. The DAC outputs to the aperture and suppressor grids go through an inverting amplifier configuration with a gain of -3.3, resulting in an output voltage range of 0 to -9.9 V.

The DAC uses a 2-wire I2C (inter-integrated circuit) compatible serial interface that is operated in the fast mode (maximum clock rate of 400 kHz). The microcontroller can uniquely set

the voltage on each grid by transferring the 16-bit values to the DAC on the active edges of the clock. The chip includes a pin-configurable I2C slave address, and also a power-on reset feature that sets all the grids to 0 V when the REDD sensor is powered on. The DAC takes 9.1 μs to settle, which is insignificant compared to the time interval between successive sample points in a 128 point one second-long IV curve sweep.

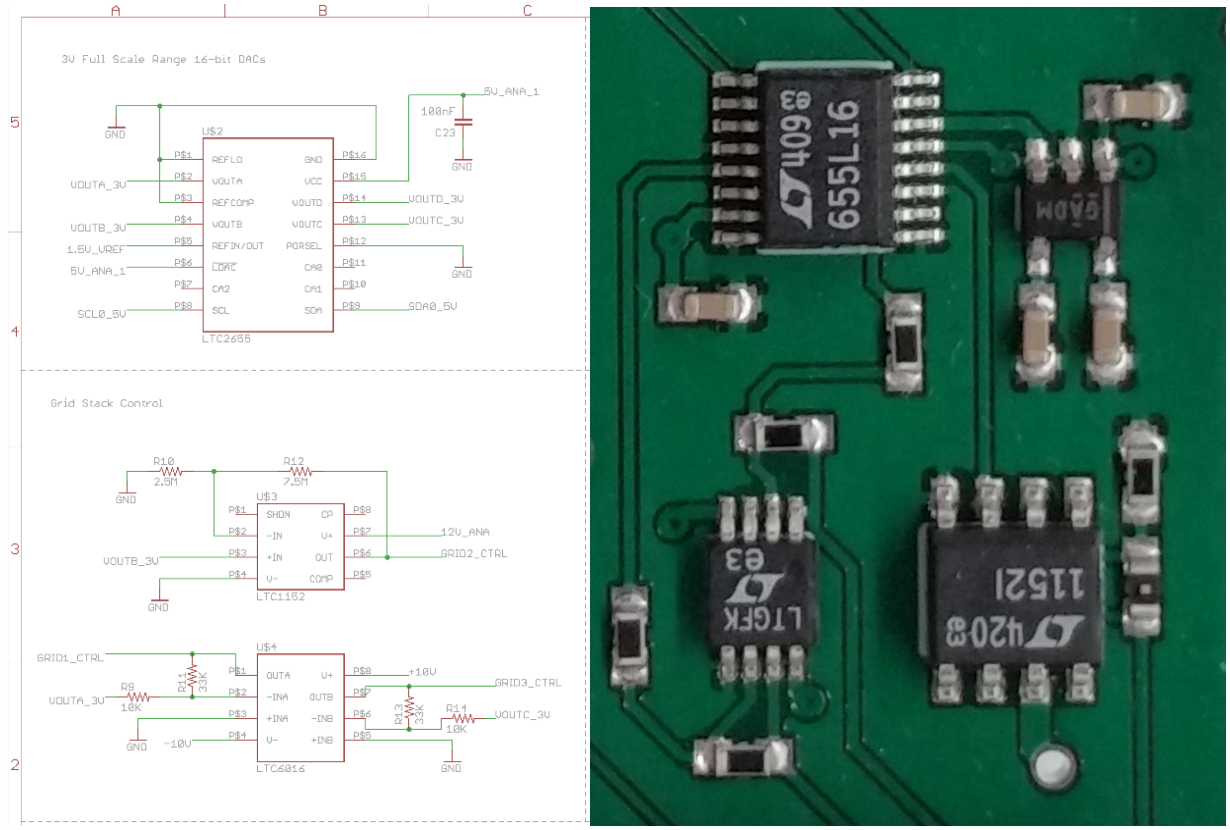

Figure 5: The left panel shows the grid control schematic, and the right panel shows a photograph of the built up circuit.

Microchannel Plate Control

Figure 6 shows the MCP control circuit design. The MCP is electrically wired in the positive ion detection mode with the phosphor screen biased at -100V, input of the assembly at -2kV and output of the assembly grounded. The large negative bias voltages for the MCP are generated by DC to DC converters that occupy less than one tenth of a cubic inch of volume. These converters are ideal for battery powered applications requiring minimal size and weight, which makes them a good choice for satellite instrumentation. The devices feature a separate high impedance programming pin and operate directly from 5 V input. The output voltage is proportional to the programming voltage (0 to 5 V produces 0 to full scale output) and features excellent linearity. The output power rating of the converters is 1 watt, which is sufficient for the REDD application.

The programming voltages for the DC to high-voltage DC converters are generated by a four-channel 16-bit DAC similar to the DAC used for grid control, but with an output full scale range of 0-2.5 V. An external reference of 1.25V is required to achieve ±0.05% accuracy. Each

DAC output is amplified by a factor of 2 using a simple non-inverting op-amp configuration, making the output voltage range 0-5 V for each channel. This DAC also operates via a serial I2C interface with the microcontroller, but it is configured to have a different slave address via the chip address pins in order to prevent serial bus conflicts.

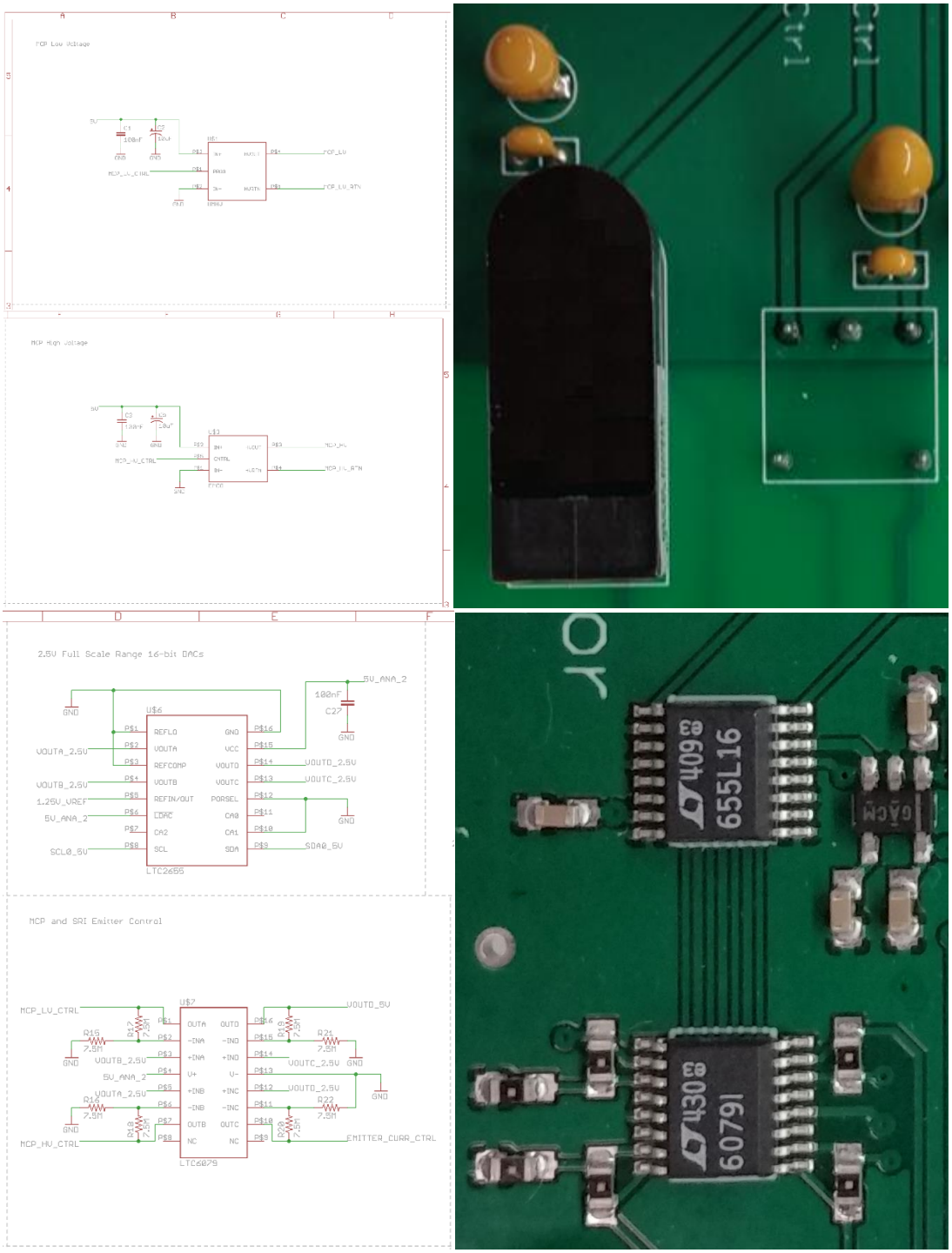

Figure 6: The left panel shows the MCP control schematic, and the right panel shows a photograph of the built up circuit.

Emitter Control

The circuit for controlling the emitter tips is provided by SRI International Corp., and its detailed schematic is included in Appendix A. The circuit takes in two control inputs for its normal operation, plus the main 5 V power supply. The enable signal turns on/off the circuit, enabling power saving functionality. The emitter current control signal regulates the current flowing through the emitter tips by applying a voltage between 0-4 V to this input, with 4 V corresponding to the full-scale current of 150 μA. This control voltage is derived from one of the channels of the DAC that generates the programming voltages for controlling the high voltage converters that bias the MCP. The circuit has three outputs, one of which is connected to the emitter tips to provide the emitter bias voltage. The other two measure the emitter voltage and emitter current, enabling closed loop emitter control. The measured emitter voltage and current outputs proportionally map the ranges of the current and voltage in the emitter tips to voltage signals with a 0-4 V full scale range. These voltage signals are digitized by two different channels of a 4-channel, single-ended, 16-bit delta-sigma ADC. An external voltage reference of 2.5 V is generated from a 5 V supply. The digitized samples are clocked into the microcontroller through the common shared I2C interface for monitoring and closed loop control in software.

Current Measurement

The primary REDD measurement is the ion current from the MCP as a function of the retarding grid voltage. Originally the LOG114 logarithmic amplifier was selected, which outputs the logarithm of the ratio between the input current and a reference current, and produces a response of 0.35 V per decade of gain. It is able to accurately output current ratios at input currents ranging from 100 pA to 10 mA. When the MCP detector current was examined with a digital multi-meter, it was noticed that this current is an electron current whose direction of flow is opposite to that of the conventional current. Since the LOG114 functions only with positive input currents, current inversion circuitry needs to be incorporated in the logarithmic current measurement chain. This increases the overall noise figure of this block, and at the same time introduces leakage currents through the board substrate that might interfere with the MCP electron current. Taking this into account along with the reduced resolution, limited current measuring capability and the need for current inversion circuitry in the case of a logarithmic transimpedance amplifier, a linear current measurement unit was designed for the REDD instrument.

Figure 7 shows the current measurement circuit design. The linear current measurement chain consists of an operational amplifier in transimpedance configuration cascaded with a low-pass filter and an ADC. They are mounted on a separate current measurement board that is connected to the main board through wire bundles. The operational amplifier chosen is the Texas Instruments LMP7721 (3-femtoampere input bias current precision amplifier), which outputs a positive voltage signal that is a linear multiple of the input electron current and the feedback resistor. The output range of this amplifier, which is connected to the next stage (low-pass filter) in the current measurement chain, is 0 V to 2.5 V. The measurement accuracy at the low end of this current range is limited by factors such as the input bias current of the amplifier, the resolution of the ADC, the input signal noise level, etc. These factors reduce the useful range of outputs from the TIA. In order to measure lower currents, an AGC (automatic gain control) scheme was implemented. This ensures that the system meets the full dynamic range requirements of the input current. The AGC scheme involves controlling the TIA's I-V gain through a switched resistor network in the feedback path. The AGC scheme yielded a better dynamic range with good linearity

primarily because there is more gain up front, which in turn reduces the overall noise figure of the cascaded chain. The voltage output from the TIA after filtering is fed into an on-chip 16-bit successive approximation ADC, configured to have a sampling rate of 30 ksps. The resolution of the ADC is ~0.4 pA at the low end of the linear range and ~0.4 nA at the high end, in compliance with the accuracy requirement shown in Chapter 2.

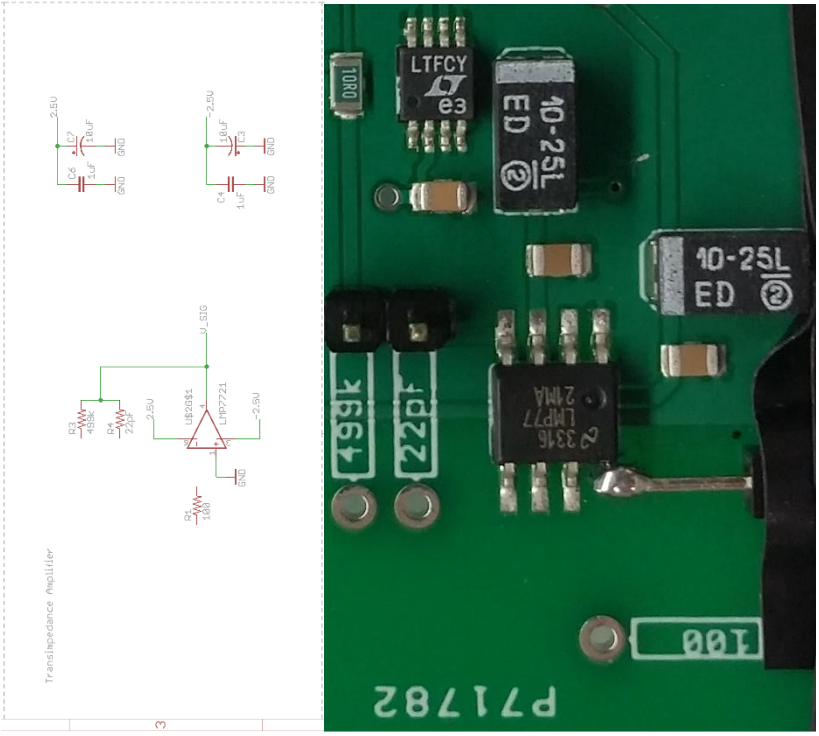

Figure 7: The left panel shows the current measurement schematic, and the right panel shows a photograph of the built up circuit.

Chapter 4-Microcontroller Design

The integrity of IV curves can vary significantly for a given space experiment based on geophysical conditions, spacecraft charging, and gradual degradation of the orbit. These factors make it advantageous to have flexibility in how the samples are spaced throughout a single RV sweep. The REDD sensor is therefore designed such that the voltage values applied to the retarding grid and the rate at which samples are taken are all configurable via software. The retarding grid voltage values are programmable, as are the number of points in a sweep and the oversampling. Based on how many points are in the sweep, the oversampling, or number of current measurements the REDD sensor accumulates before averaging, changes. In addition, the amount of time that the REDD instrument waits between updating the grid voltage and taking current samples changes depending on the number of points per sweep. In all cases this time is larger than the settling time for the grid voltage.

The main functions of the microcontroller are to control the timing of the DAC and ADC conversions, and to send data back through the USB serial communication interface to a computer or other device. Table 2 lists the default values of the parameters that can change depending on the firmware in the flash memory of the microcontroller.

Parameter	**Default Mode**
Sweep voltage setting	Uniformly spaced points over 0-12 V
Points per sweep	128
Oversampling	30
Voltage on Aperture and Suppressor Grids	Held at 0 volts
Wait time between setting DAC and measuring current	252 μs

Table 2: REDD sensor default operating mode. The total time for a full retarding voltage sweep is 1 second.

Communication

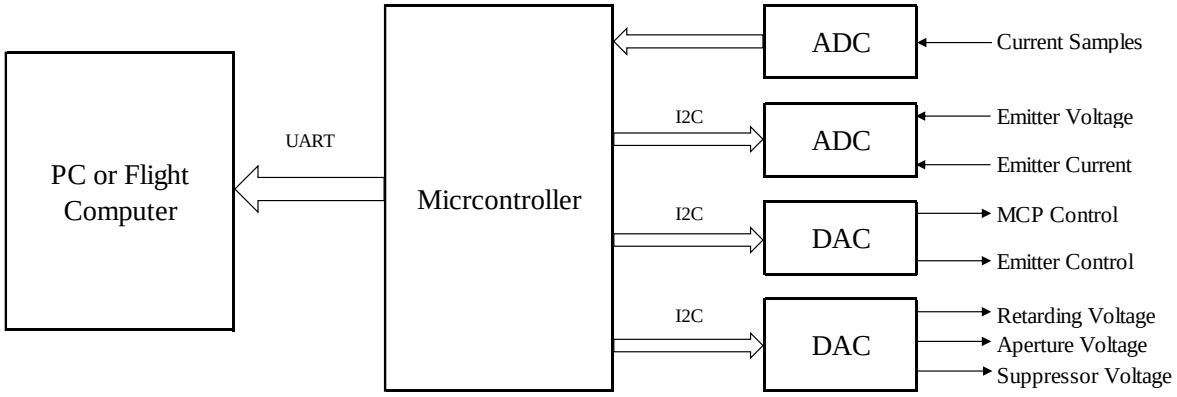

Figure 8: Interconnect diagram of the REDD sensor electronics.

The microcontroller is connected to a computer through a serial communication interface that interfaces the microcontroller's UART (universal asynchronous receiver/transmitter) to the computer's USB (universal serial bus). The microcontroller is always sending bytes of data

through this interface, whose configurable baud rate has a default setting of 115200 bps. With this data rate, there is ample time between successive points in the RV sweep for all four data bytes that comprise one point on the I-V curve (two bytes for a current sample and two bytes for a voltage sample) to be transmitted before the next point begins.

Serial Interfaces

The communication between the 16-bit ADC, DAC and the microcontroller is accomplished through an I2C serial interface. The microcontroller sends 16-bit values to the DACs using the 400 kHz I2C system clock. When it is time to update a grid voltage in a sweep, the microcontroller sends a command to the DAC that includes the channel it is updating and the 16-bit value. As it is a linear step, the step size is added to this value after each point. A DAC command transmission takes about 80 μs. The data output from the 16-bit ADC is shifted out on the active edges of the clock over a 60 μs period.

Timing

The microcontroller must be able to properly time the retarding voltage grid updates and current samples so as to have enough time for the system to respond after the grid voltage is changed, while maximizing the current oversampling for the selected number of points per sweep. The timing scheme must also allow sufficient settling time so that the current measurement is not affected by switching transients. A diagram of the timing of a 128-point sweep is shown in Figure 9. Between setting the DAC and taking current samples for each point the microcontroller waits 252 μs. For each point in the sweep, the microcontroller sends a command to the DAC telling it to set the retarding grid to the next voltage in the sweep. After setting the grid voltage, the microcontroller also waits for the linear transimpedance amplifier to respond. After 252 μs the microcontroller oversamples and averages the current samples, with the samples distributed uniformly in the remaining interval of time. When this is complete, it reconfigures for the next sample by setting the DAC (retarding voltage) to its new value. It repeats this process until it has taken 128 points as per the default sweep mode, taking a total of about 999.936 ms for each sweep.

In a uniform 128 point RV sweep, the maximum time interval between any two successive sample points is 7812.5 μs (1s / 128). Since the ADC oversampling of 30 samples needs to be uniformly distributed in this time interval, the time difference between any two consecutive ADC samples and the time interval between setting the DAC and the first ADC sample in any one particular point of a 128 point RV sweep needs to be 252 μs (7812.5μs / 31). Keeping this as the main design input for the timing scheme, one of the microcontroller's timers is configured to repetitively measure a period of 252 μs and generate an interrupt at the end of each period. Hence a one second long RV sweep will contain 3968 interrupts (128 x 31) with the first interrupt aligned to time t = 0 s and the last interrupt at time t = 1 s. Starting from the first interrupt, on every 31st interrupt the microcontroller sends a command to the DAC telling it to set the retarding grid to the next voltage in the sweep. On the remainder of the interrupts, the ADC samples will be taken, and 30 samples averaged pertaining to every sample point in a 128 point RV sweep.

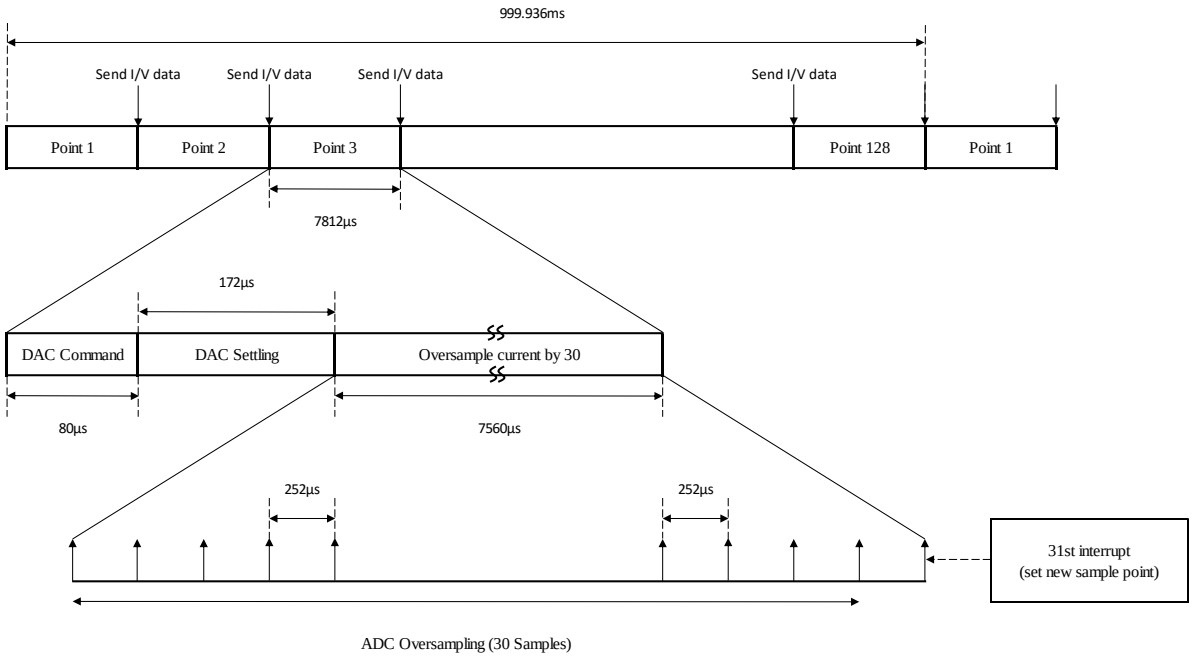

Figure 9: Timing diagram of the default 128-point REDD sensor sweep

Based on the system requirements, a simple scalable timing scheme has been developed to properly time the retarding voltage grid updates and current samples for the best possible system response. In the next chapter the performance of the REDD sensor electronics is discussed in detail.

Chapter 5-Validation

Performance Summary

A photo of the assembled REDD electronics is shown in Figure 10. A summary of the REDD sensor theoretical performance compared with its requirements is shown in Table 3. These parameters are for a particular scenario and it is easy to change several of the parameters given different scenarios. For instance, the sweep time and points per sweep can be changed easily by using a different microcontroller algorithm. The resolution can be improved by oversampling and averaging to add more bits of precision. The voltage ranges of the grids can be controlled by changing the microcontroller software, within the full scale range constraints. The current range can be changed by changing the I-V gain of the TIA through its feedback resistance, or by altering the bias voltages of the MCP in order to change its electron current gain, or by adjusting the voltage on the emitter tips, which in turn would control the efficiency of the ionization process.

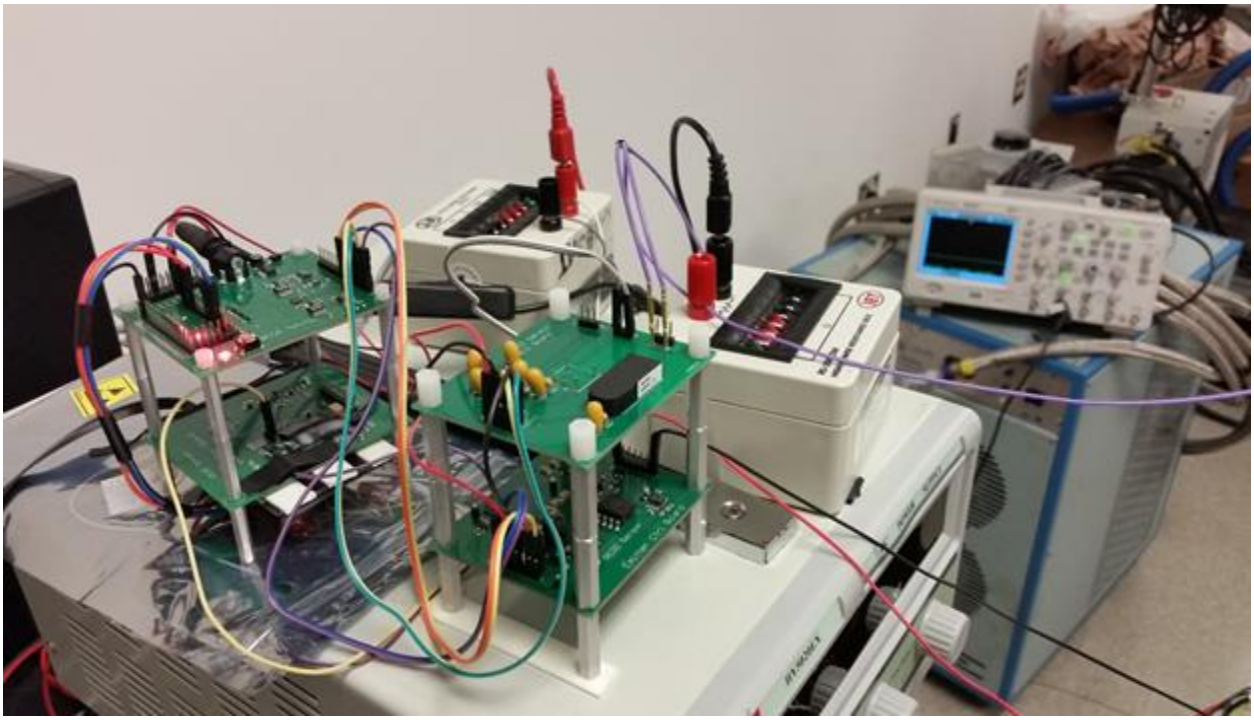

Figure 10: Photo of assembled REDD electronics boards

Parameter	**Requirement**	**Design Expectation**
Measured Current Range	100 pA to 10 μA	100 pA to 10 μA
Measured Current Accuracy	Greater of 100 pA or 2.5 %	0.4pA to 0.4 nA
Samples per I-V Curve	128 or More	128
I-V Curve Sweep Time	1 s or More	1 s
Retarding Voltage Range	12 V or More	0 to 12 V
Suppressor Bias	-5 V or Less	0 to -9.9 V
Aperture Bias	0 V or Less	0 to -9.9 V
Survival Temperature	-20° to 75° C	-20° to 75° C

Table 3: Summary of the REDD sensor performance

Bench Testing of the REDD Main Board

The first testing that was performed on the main board was a bench test run-through to validate all the hardware and the microcontroller. After the main board was plugged in to the external power supply of 12 volts, the 5 V, 3.3 V and ±10 V board-generated power supplies along with the 1.25 V, 1.5 V, 2.5 V and 3 V board-generated voltage references were verified.

The 16-bit DACs and the 16-bit ADC were tested by loading the microcontroller with a code specially written for debugging. With this code burnt into the flash memory of the microcontroller, individual UART commands were able to control each part on the board separately, or all parts together. Every DAC channel's final output was tested and verified by doing two different sets of tests. The first test was a 64-point linear DAC sweep, with the output voltage measured at each step using a multi-meter. These measured voltages were then compared against the ideal expected voltages, calculated from the DAC's resolution, its reference voltage and the external amplification factor.

The second test was a one second long 128-point full-scale linear DAC sweep, whose waveform attributes were captured using an oscilloscope. The ADC was tested by sending commands to sample different channels and return one 16-bit sample. All four channels of the ADC were verified by taking the output of the DAC channel that has 0-5 V full-scale range and connecting it to each ADC channel's input, one at a time in a loopback fashion. The DAC output voltage was linearly swept over its full range while reading the ADC output values corresponding to each input. Figures 11-25 show the linear sweeps for all test-points on the REDD main board. As is clear from the figures and table, all of the voltages controlled by the DAC outputs and regulators are linear over the range of interest, which allows the micro-tip emitters, grids, MCP, and extraction plates to be adjusted to control the functions of the REDD instrument.

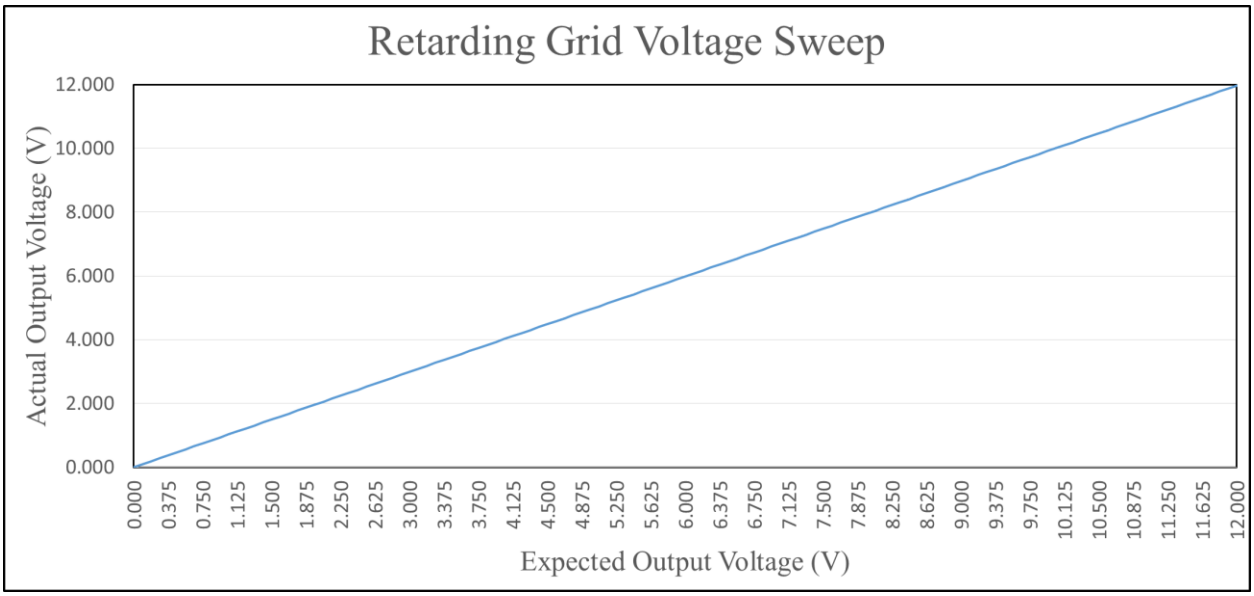

Figure 11: Voltage data from the circuit board during a 128-point linear sweep.

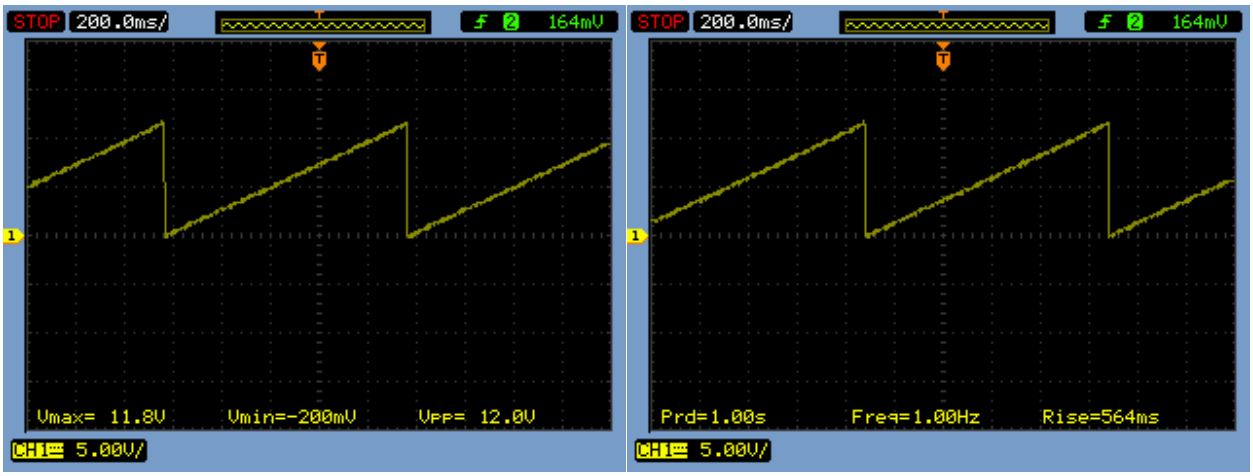

Figure 12: Oscilloscope measurements of retarding grid voltages during a 128-point linear sweep.

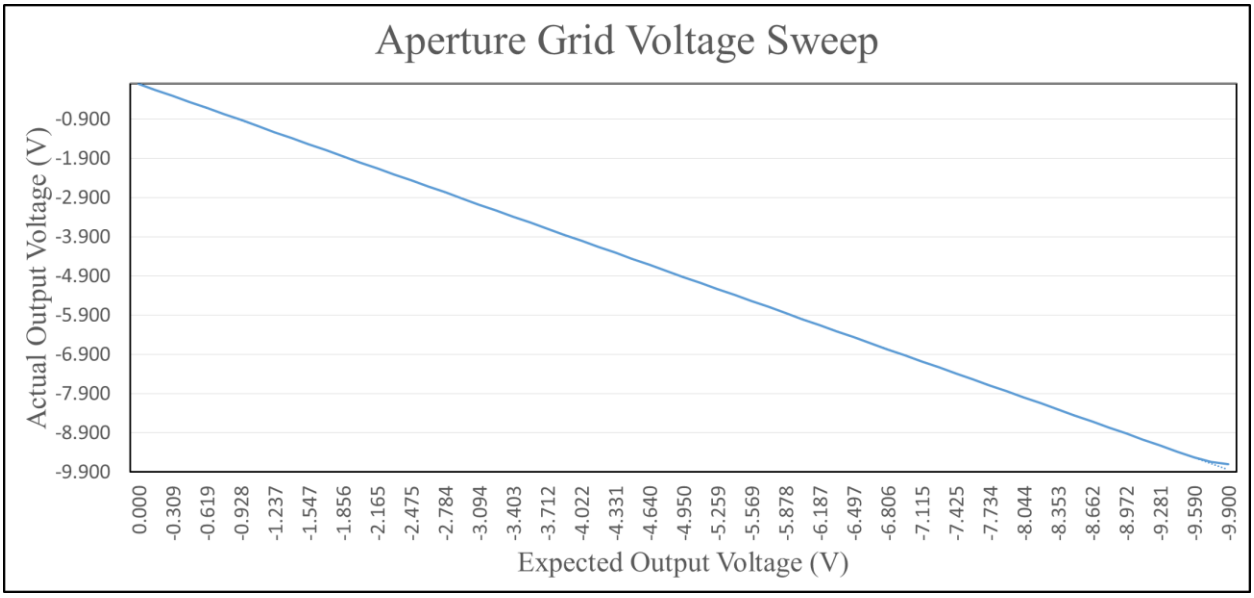

Figure 13: Voltage data from the circuit board during a 64-point linear sweep.

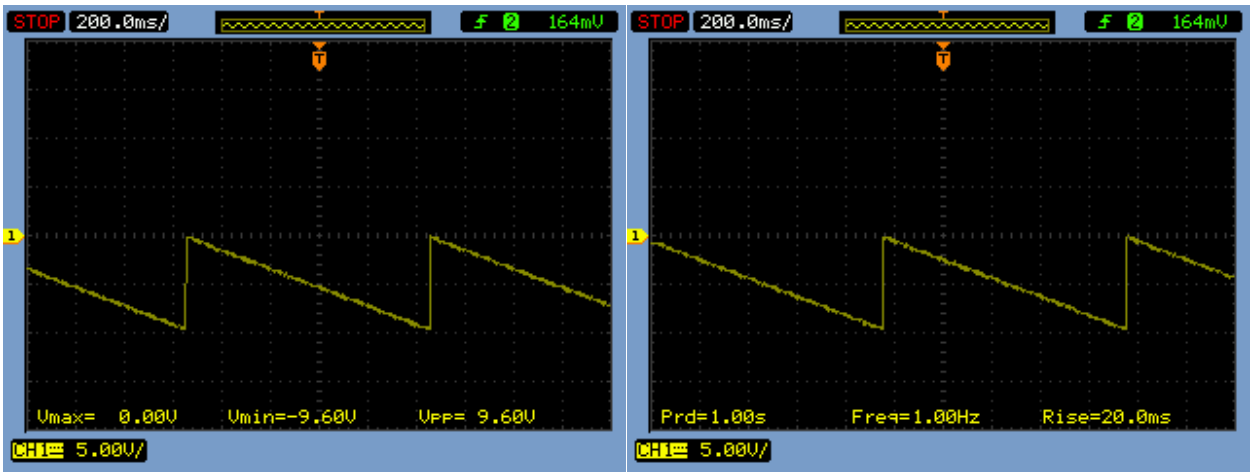

Figure 14: Oscilloscope measurements of aperture grid voltages during a 128-point linear sweep.

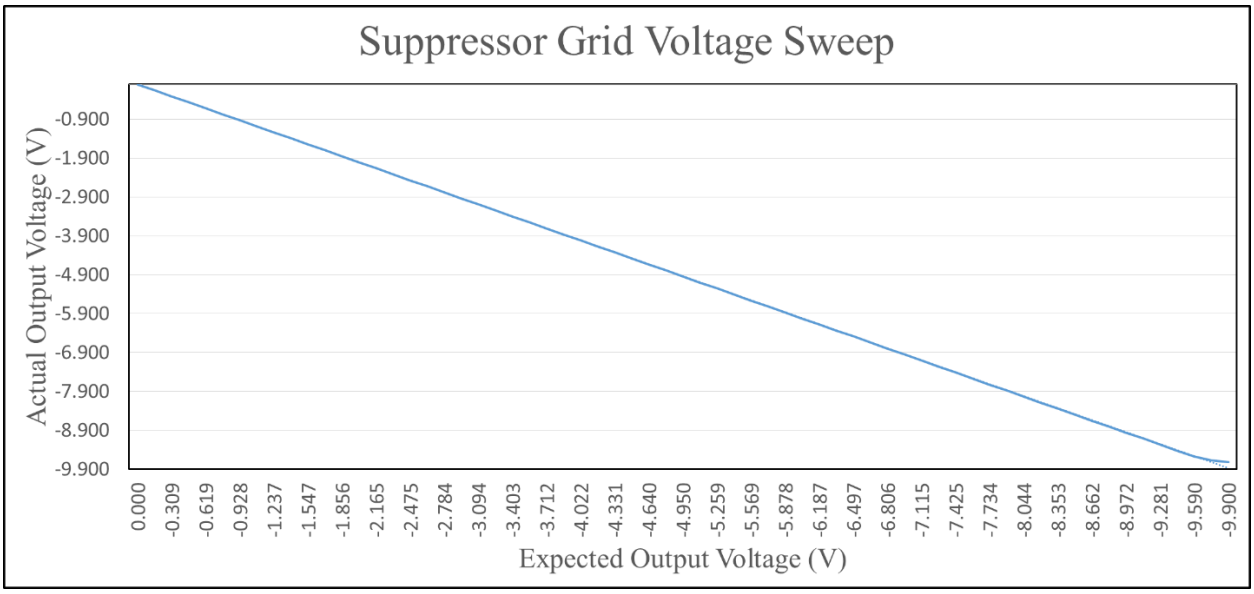

Figure 15: Voltage data from the circuit board during a 64-point linear sweep.

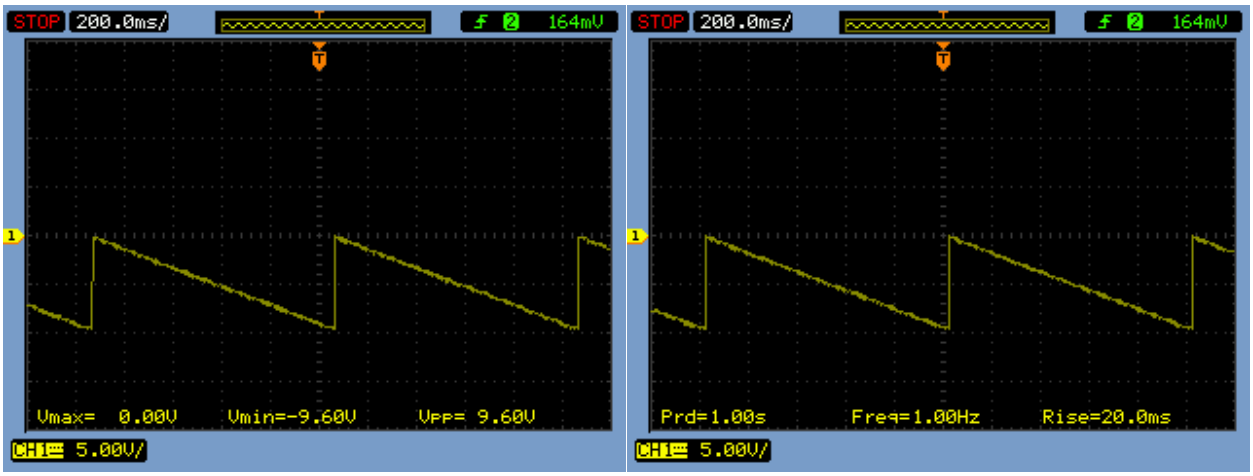

Figure 16: Oscilloscope measurements of suppressor grid voltages during a 128-point linear sweep.

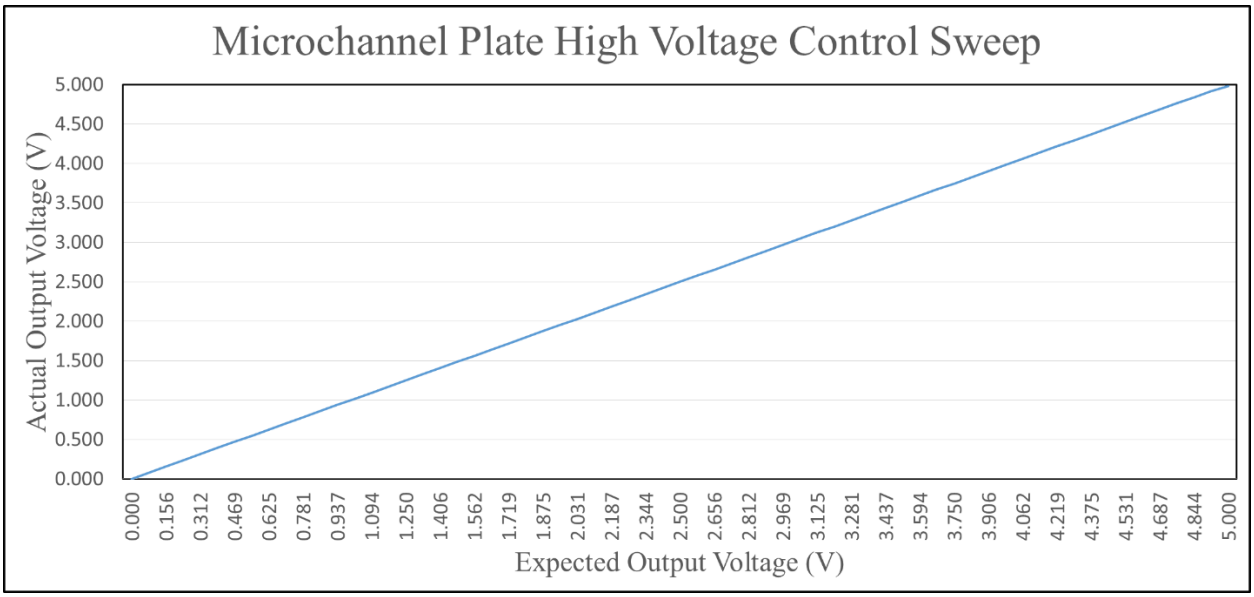

Figure 17: Voltage data from the circuit board during a 64-point linear sweep.

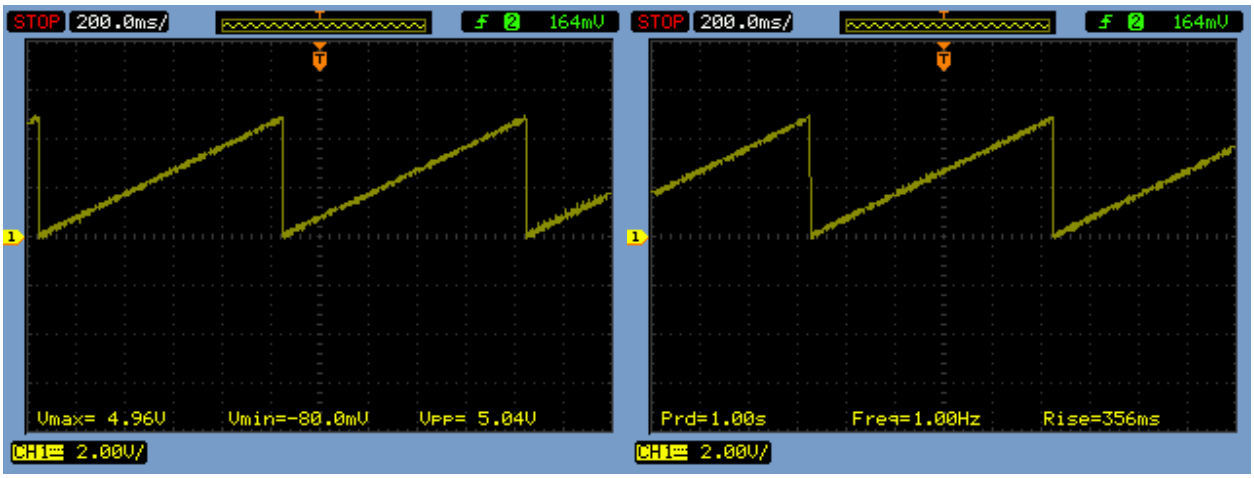

Figure 18: Oscilloscope measurements of microchannel plate high voltage control voltages during a 128-point linear sweep.

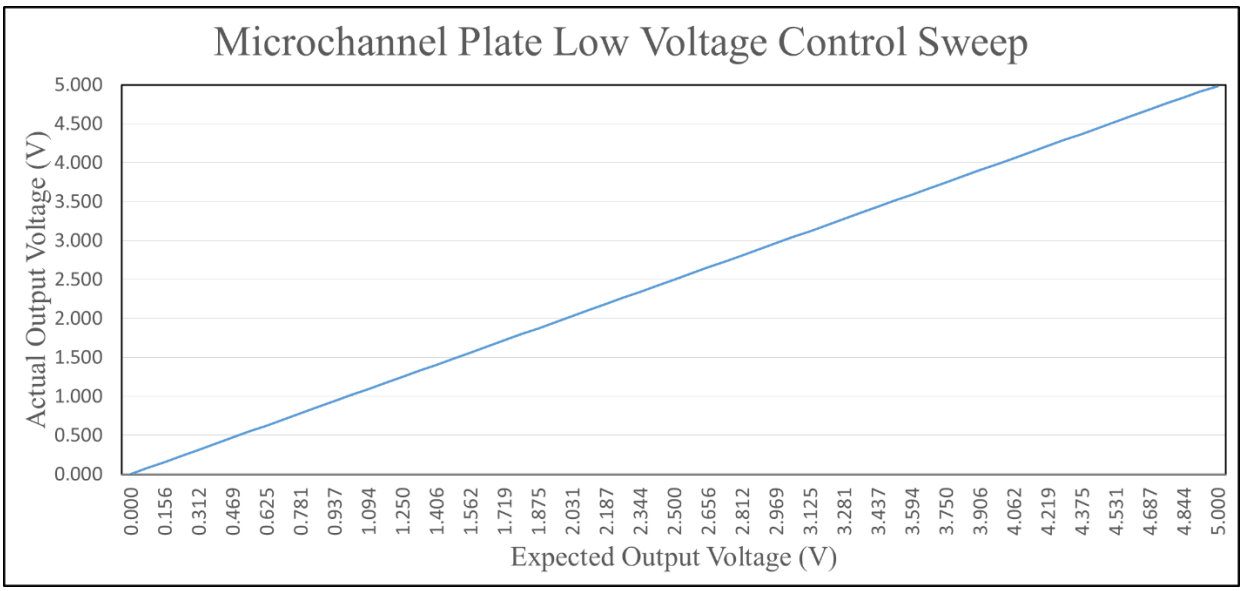

Figure 19: Voltage data from the circuit board during a 64-point linear sweep.

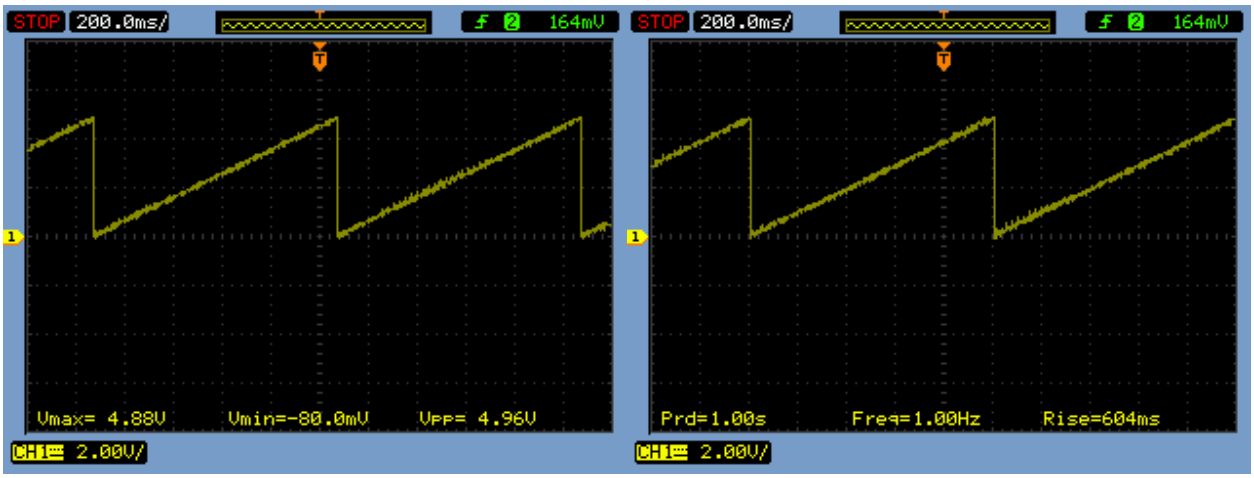

Figure 20: Oscilloscope measurements of microchannel plate low voltage control voltages during a 128-point linear sweep.

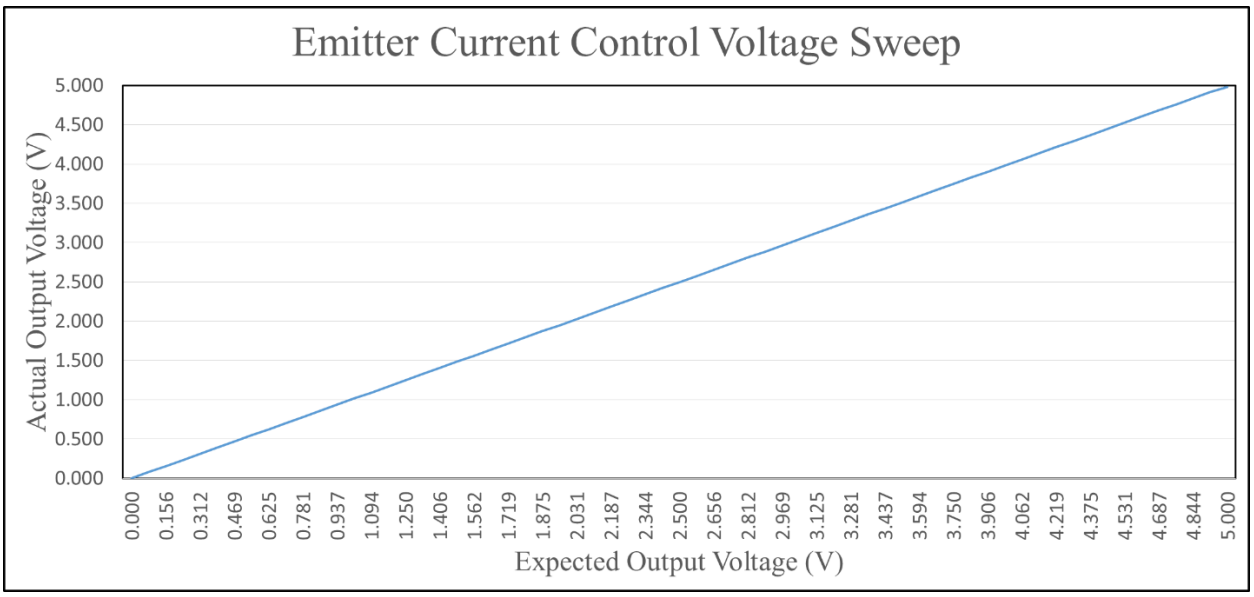

Figure 21: Voltage data from the circuit board during a 64-point linear sweep.

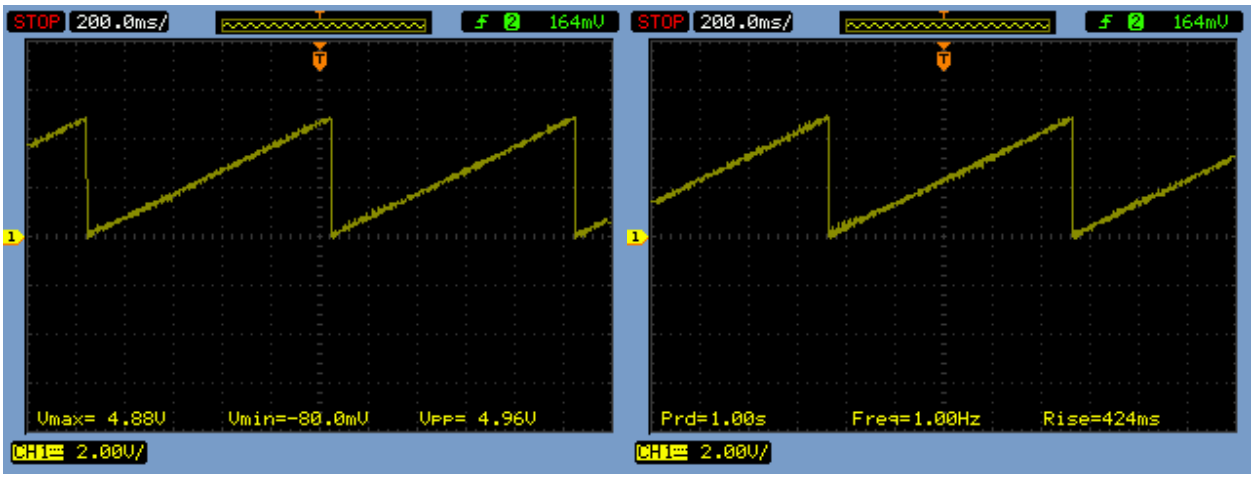

Figure 22: Oscilloscope measurements of emitter current control voltages during a 128 point linear sweep.

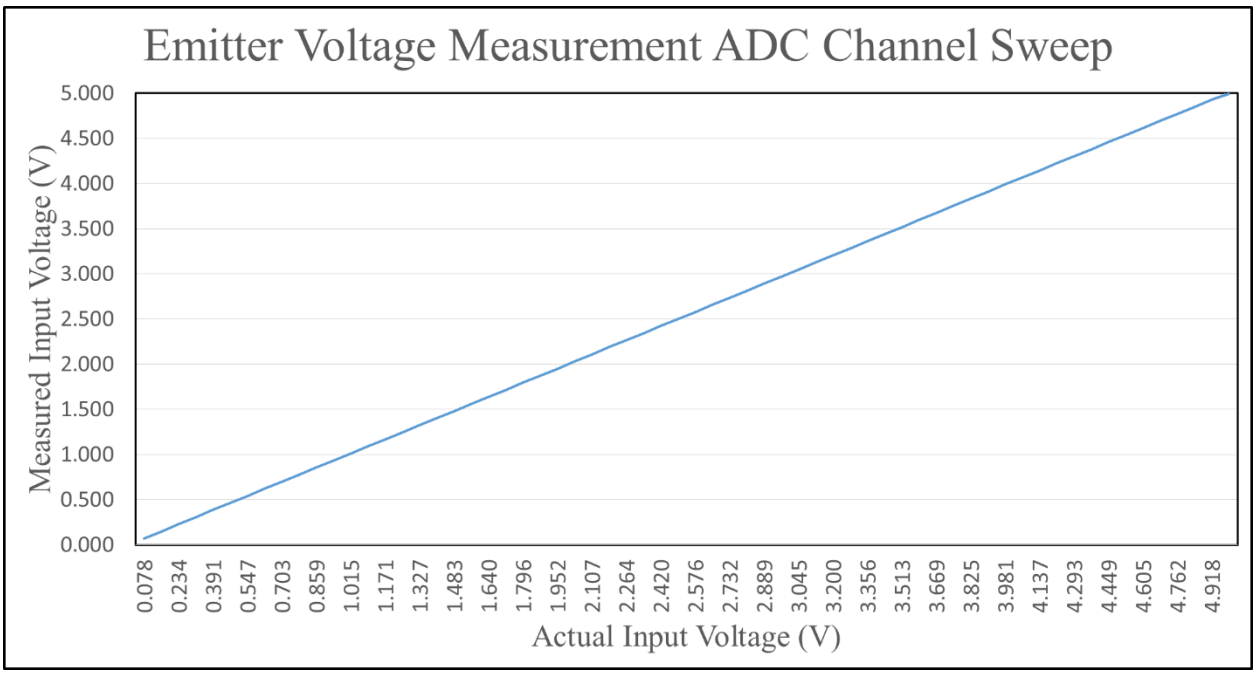

Figure 23: Voltage data from the circuit board during a 64-point linear sweep.

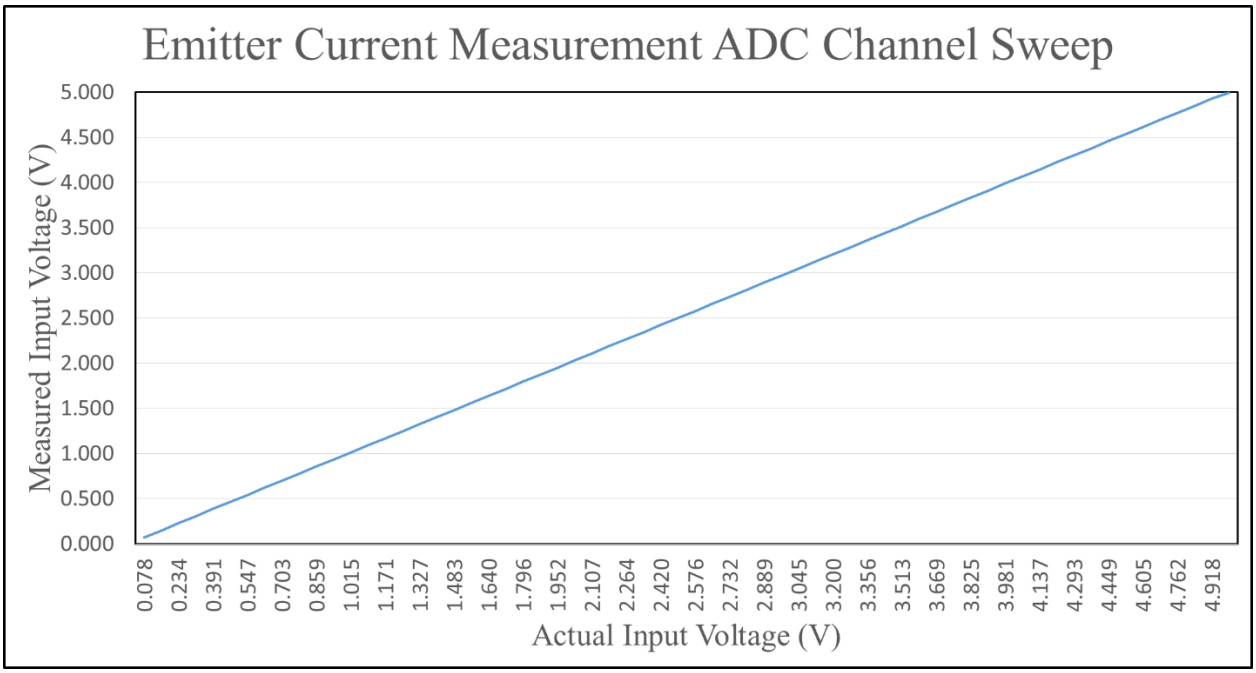

Figure 24: Voltage data from the circuit board during a 64-point linear sweep.

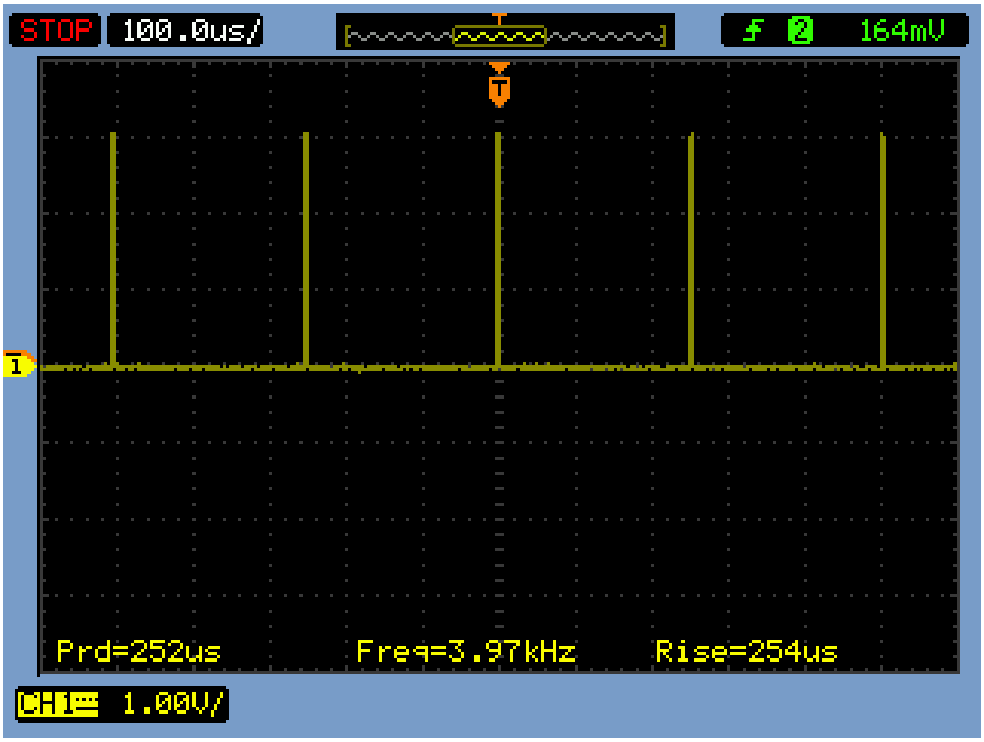

Figure 25: Oscilloscope measurements showing interrupt periodicity to validate the timing scheme of the default 128-point REDD sensor sweep.

Bench Testing of the REDD High-Voltage Converter (HVC) Board

The first testing that was performed on the HVC board was a bench test to validate all the hardware connections. After the HVC board was powered up through the 5 V power supply that is generated on the main board, the ±10 V board-generated bias voltages for the extraction plates were verified. The DC to DC converters in the HVC board for generating the large negative bias voltages for the MCP were tested and verified by connecting their respective control inputs to their corresponding control signals generated in the main board, and capturing the waveform characteristics of the load dependent output voltage of these converters on an oscilloscope, as depicted in Figures 26 and 27. The scope input is made through a high-voltage probe across a 2.5 MΩ load resistance, while stepping the respective control signals from 0 V to 5 V in a uniform 128-point linear sweep. In the figures below, the green waveform is the control signal, and the yellow waveform is the proportional voltage signal output from the converters.

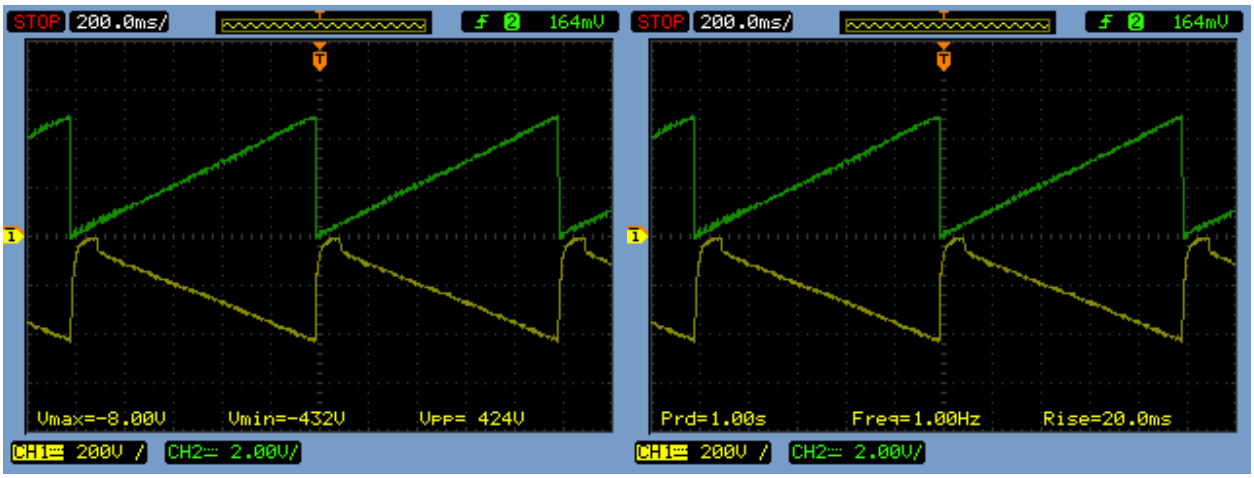

Figure 26: Oscilloscope measurements of microchannel plate low bias voltages during a 128 point linear sweep of its control signal.

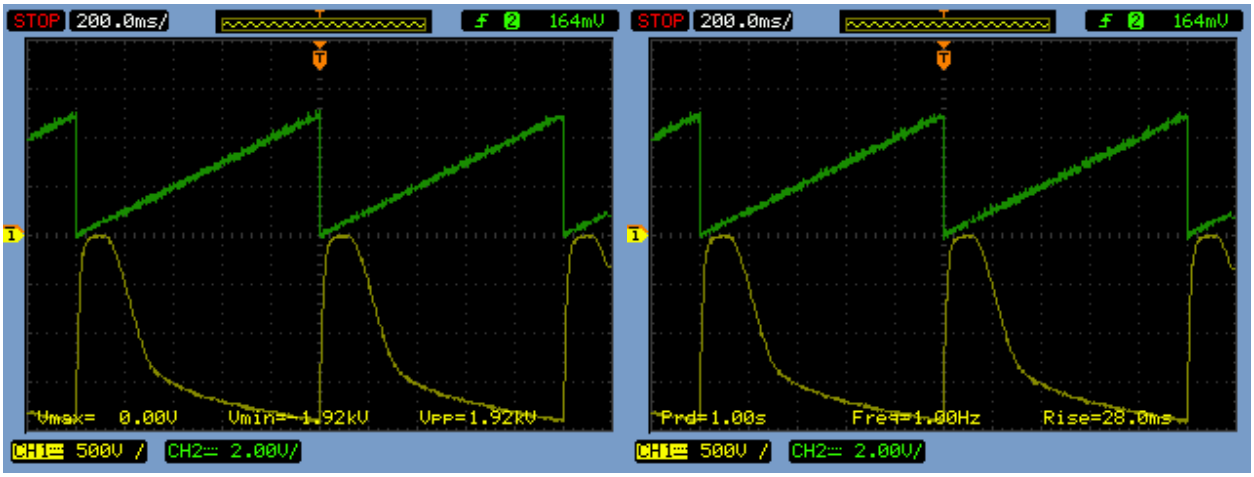

Figure 27: Oscilloscope measurements of microchannel plate high bias voltages during a 128 point linear sweep of its control signal.

In order to prevent damage to the MCP through electric arcing in the vacuum chamber, a gradual turn-on procedure for the MCP high bias voltages is implemented in the power-on

sequence for a period of 25 minutes, based on the transfer characteristics obtained in Figure 27. This MCP high bias non-linear voltage ramp up procedure is shown in detail in Table 4.

DAC Input Code	Input Control Voltage (V)	Output High Voltage (V)	Time (min)
0	0.001	-40	0
9215	0.703	-120	1
10239	0.781	-320	2
11263	0.859	-520	3
12287	0.937	-720	4
13311	1.015	-920	5
14847	1.132	-1120	6
17407	1.327	-1320	7
17919	1.366	-1360	8
18431	1.405	-1400	9
19455	1.483	-1440	10
20479	1.561	-1480	11
21503	1.640	-1520	12
23551	1.796	-1560	13
24575	1.874	-1600	14
28671	2.186	-1640	15
30719	2.342	-1680	16
32767	2.498	-1720	17
37887	2.889	-1760	18
40959	3.123	-1800	19
44031	3.356	-1840	20
47103	3.591	-1880	21
54271	4.137	-1920	22
58367	4.449	-1960	23
63487	4.840	-2000	24

Table 4: MCP high bias voltage ramp up sequence.

Bench Testing of the REDD Emitter Control Board

The first testing that was performed on the emitter control board was a bench test to validate all the hardware connections. After the board was powered through the 5 V power supply, the emitter current control signal was swept from 0 V to 5 V in a 128-point linear step, and the corresponding emitter bias voltage waveform was captured on an oscilloscope across a 499 kΩ load resistance as shown in Figure 28. The emitter voltage and the emitter current outputs were validated in the same sweep as depicted in Figures 29 and 30 respectively, by feeding these voltage signals into different channels of the 16-bit ADC on the main board, and scaling (multiply by 37.5 for the current and -50 for the voltage) the digitized outputs proportionally to obtain the measured current and voltage values.

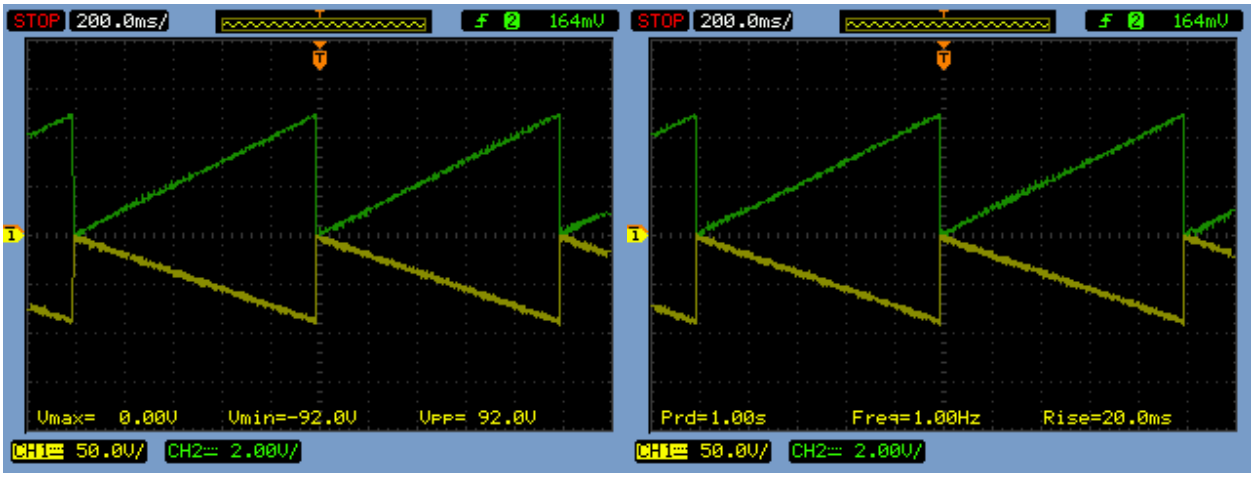

Figure 28: Oscilloscope measurements of the emitter bias voltages during a 128 point linear sweep of its control signal.

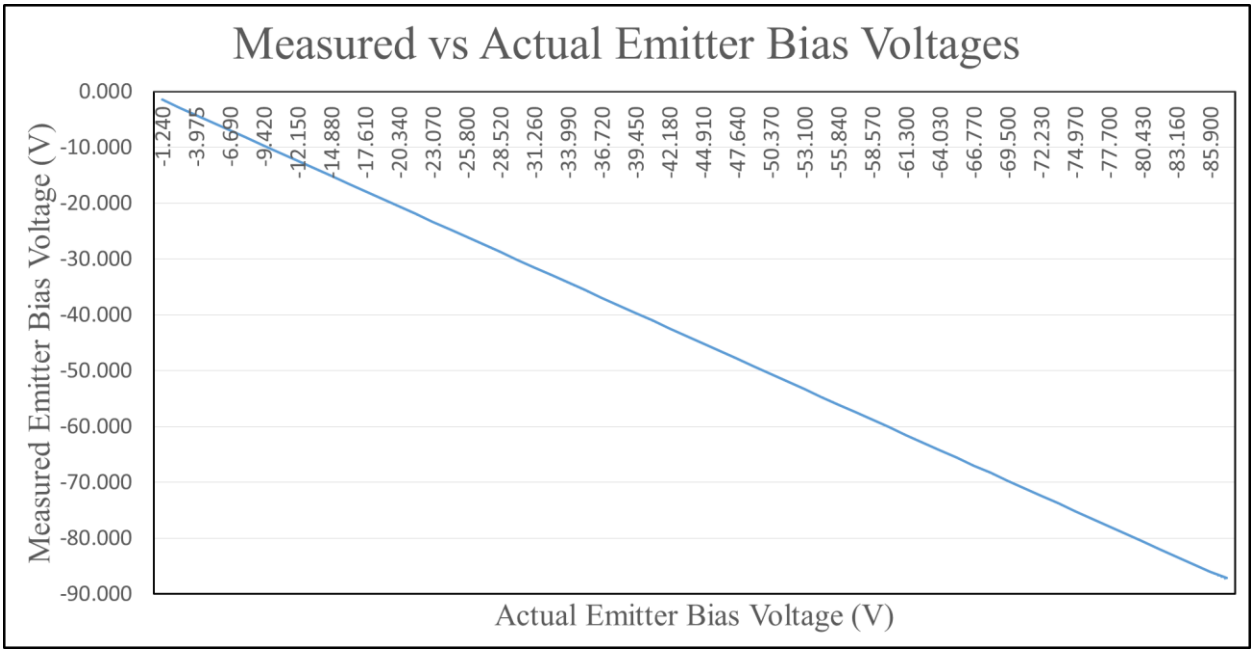

Figure 29: Measured versus actual emitter bias voltages during a 128 point linear sweep of its control signal.

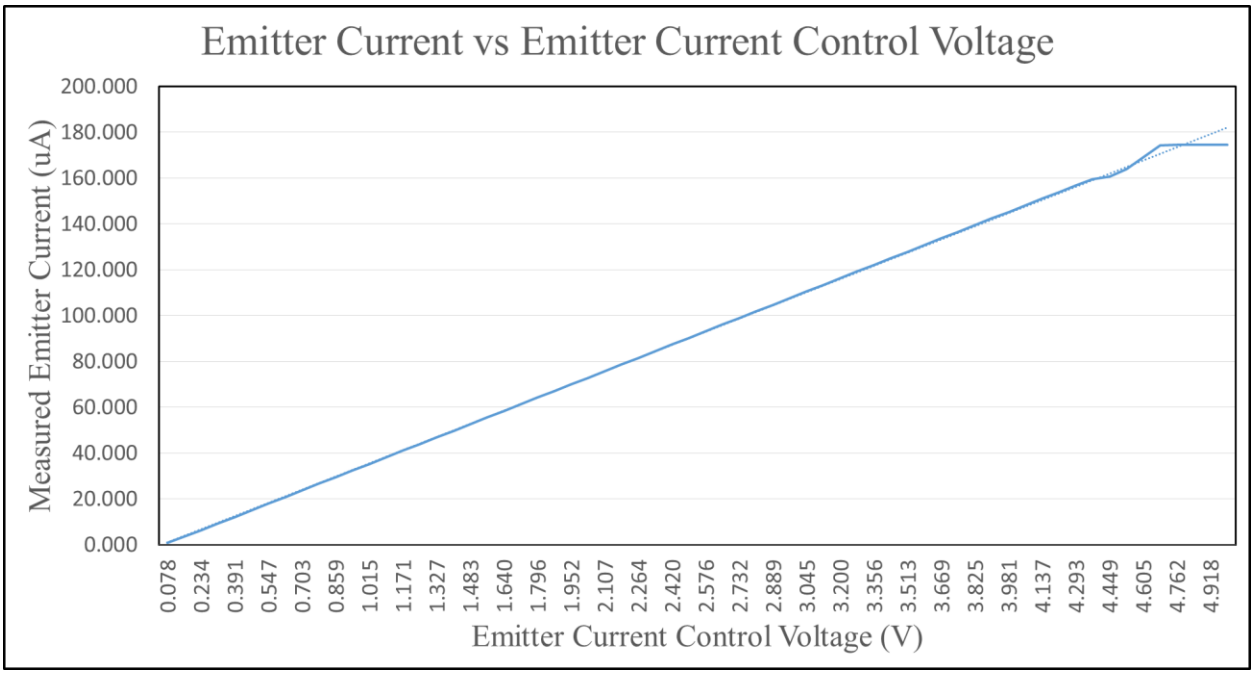

Figure 30: Measured emitter currents during a 128 point linear sweep of the emitter current control signal.

Bench Testing of the REDD Current Measurement Board

The first testing that was performed on the current measurement board was a bench test to validate all the hardware connections. After the board was powered up through the 5 V power supply, the ±2.5 V board-generated power supplies along with the 2.5 V board-generated voltage reference were verified. Figure 31 shows the voltage output from the TIA with respect to the input electron current from a precision current source for two different feedback resistances, red being 100 kΩ and green being 1 MΩ. Figure 32 shows the linear current measurement results with the AGC scheme that involves controlling the TIA's I-V gain through a switched resistor network in the feedback path (red being 100 kΩ, blue being 1 MΩ and green being 10 MΩ). This AGC scheme yielded a linear current measurement range from 1 nA to 25 μA. However, while increasing the feedback resistance in order to measure electron currents as low as 100 pA, it was observed that the voltage on the inverting input of the TIA was above virtual ground because of the parasitic resistances and inductances introduced at the inverting input junction through the usage of through-hole components, causing the TIA to deviate from its ideal I-V characteristics. The counter measures needed in order to circumvent this problem are discussed in Chapter 6.

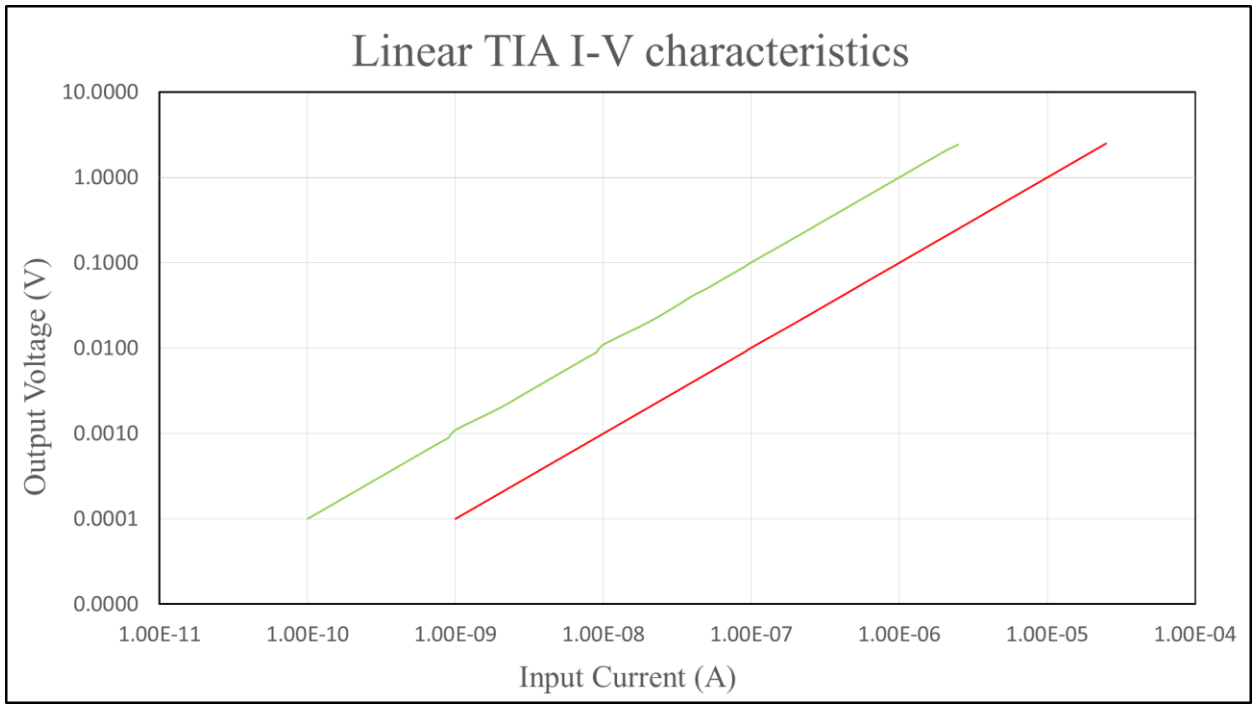

Figure 31: Linear TIA I-V characteristics for two different feedback resistances.

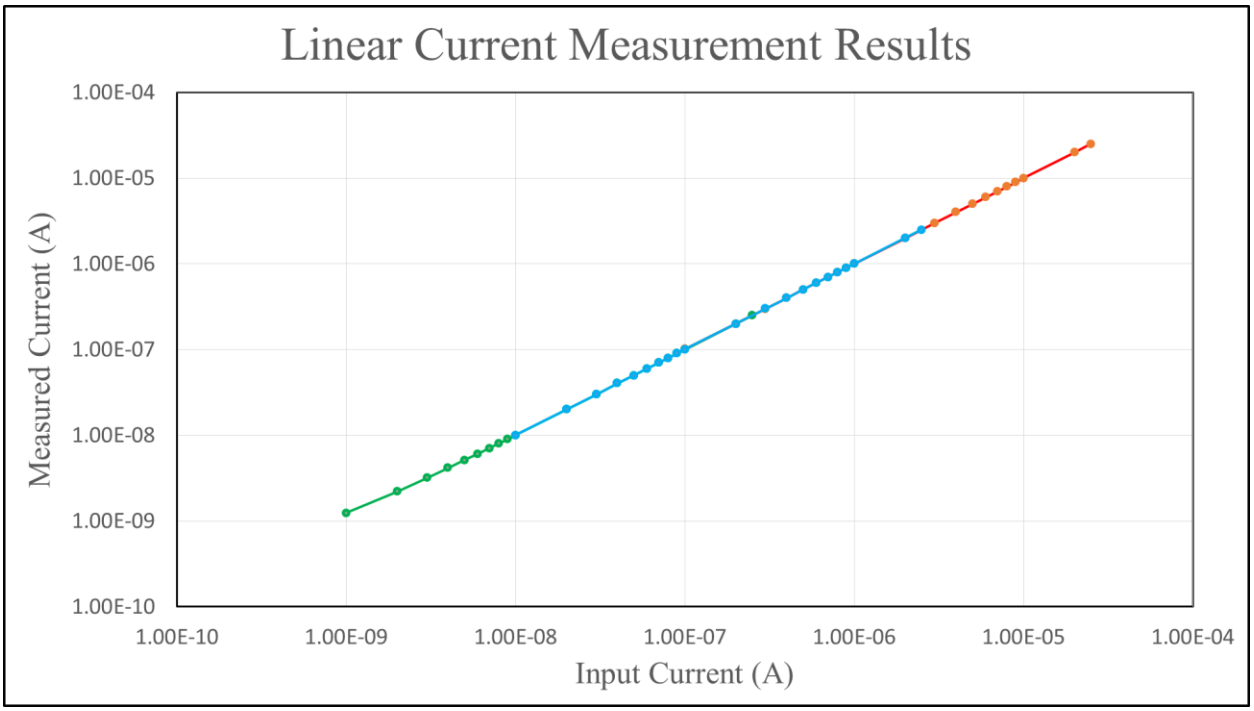

Figure 32: Linear current measurement results for different feedback resistances of the TIA.

Vacuum Testing

A diagram of the vacuum chamber test set-up for the REDD instrument is shown in Figure 33. The vacuum chamber contains an ion source directed at the MCP. The emitter tips housed within the ionization chamber are connected to the emitter control board for voltage control, and the MCP is connected to the REDD high-voltage converter board for the large negative voltages required to bias the MCP. The power and signal lines of the REDD instrument are wired through connectors at the top of the vacuum chamber to the REDD electronics outside for power and control. The four REDD boards are stacked in pairs of two and located beside the vacuum chamber, as can be seen in Figure 33.

Figure 34 shows the schematic diagram of the REDD instrument for vacuum testing. The ion source in the vacuum chamber works by ionizing neutral gas with electrons that are emitted by the emitter tips. The electrons from the emitter tips are electrostatically directed and travel towards an electron collector plate that is held at positive potential, which causes them to travel through neutral gas and ionize it. By changing the potential on the tips the distribution of the generated ions can be controlled. The ion density can also be increased by increasing the pressure in the chamber.

The first test to validate functionality of the REDD instrument is to measure the electron current from the MCP for different pressures in the chamber. Figures 35 and 36 show the MCP current measurement and the emitter current measurement respectively for different chamber pressures. As expected, the measured MCP and emitter currents grows somewhat linearly with increasing chamber pressure. It is also observed that the MCP and emitter currents decrease beyond a particular pressure value due to degradation of the emitter tips at higher pressures. Figure 37 shows the plot of the ratio between the MCP and emitter currents for different chamber pressures. Ideally this should be flat, but based on the characteristic of the plot obtained in Figure 37 it can be inferred that the sensor behavior is fairly uniform over the range of pressures. This shows that the MCP and emitters are scaling together as we want them too. All these plots indicate that the REDD electronics is functional and able to capture ions and measure them as a current.

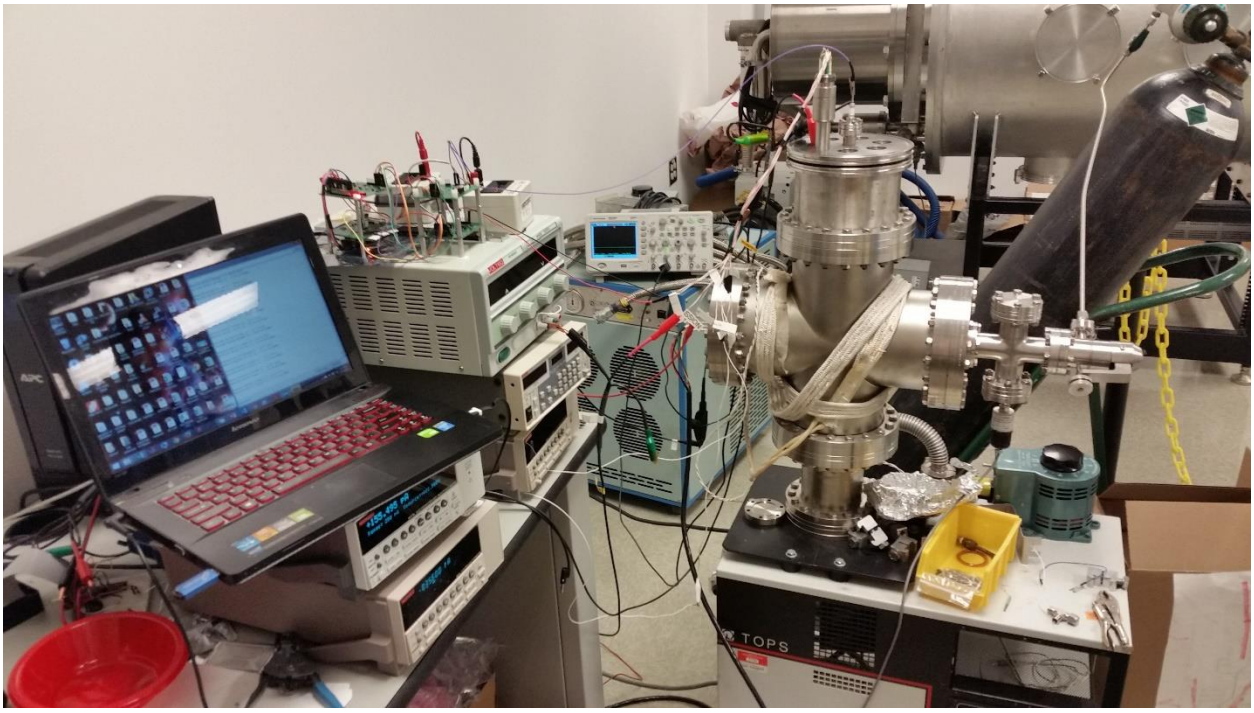

Figure 33: Vacuum chamber test set-up of the REDD instrument.

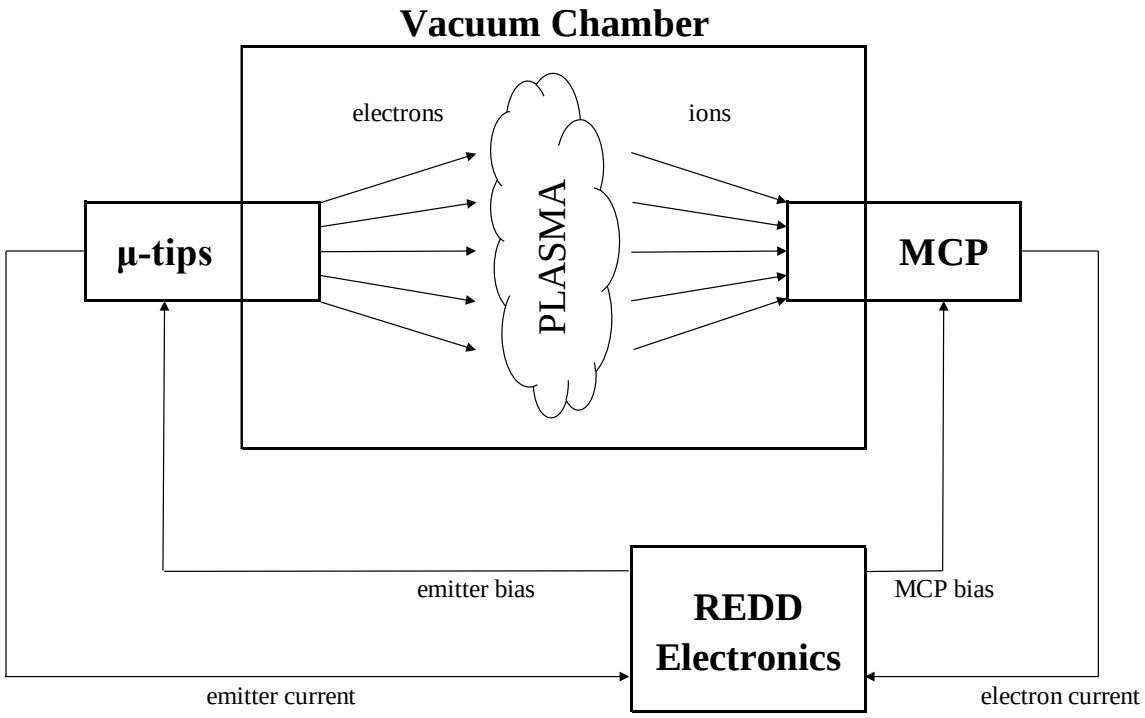

Figure 34: Vacuum chamber schematic diagram of the REDD instrument.

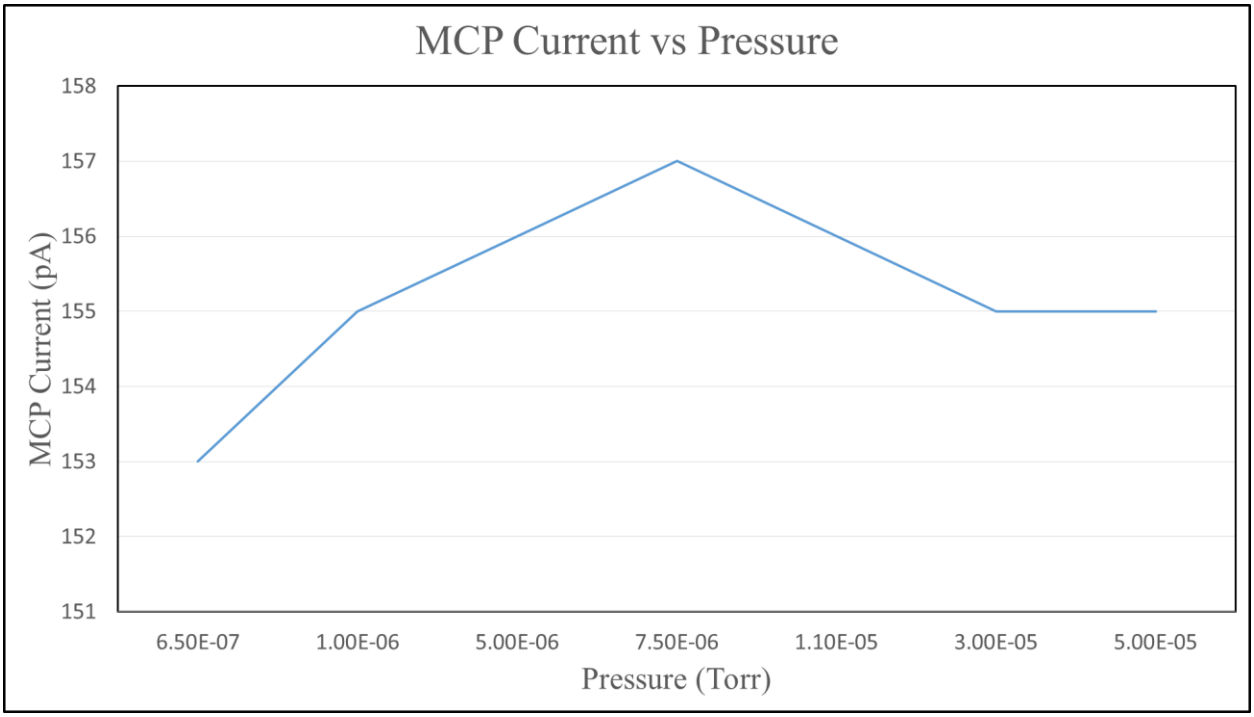

Figure 35: MCP current measurements for different chamber pressures.

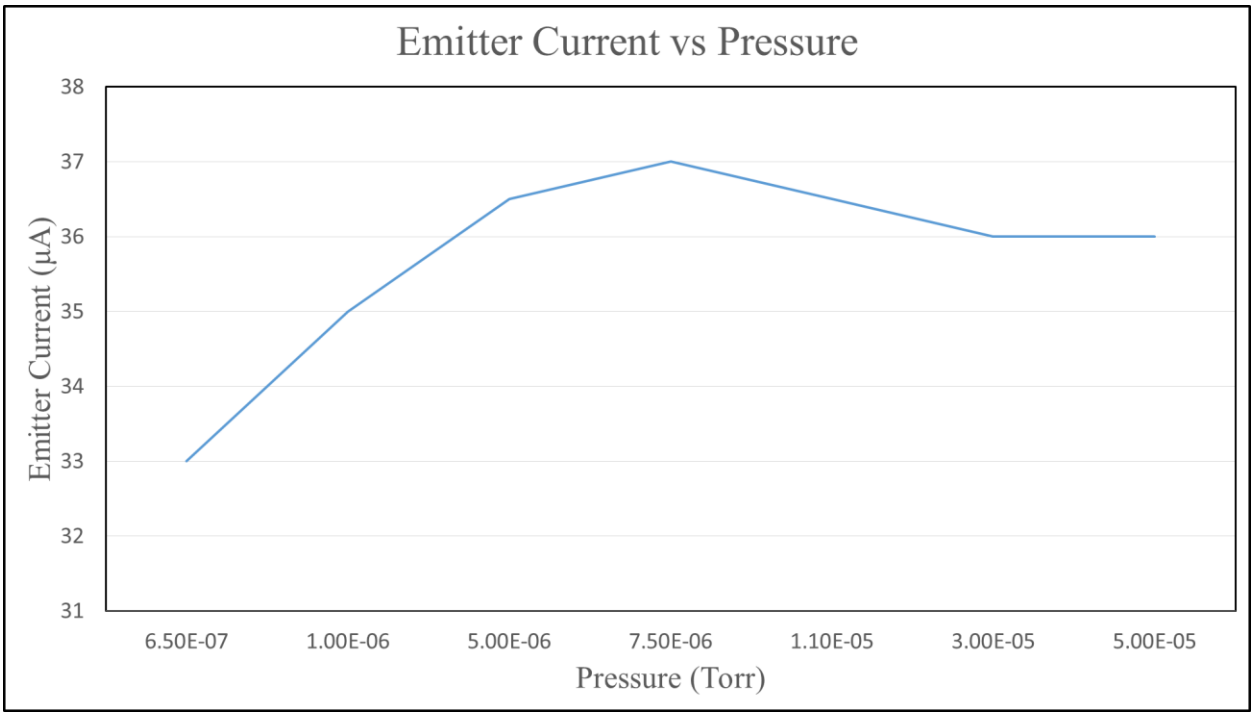

Figure 36: Emitter current measurements for different chamber pressures.

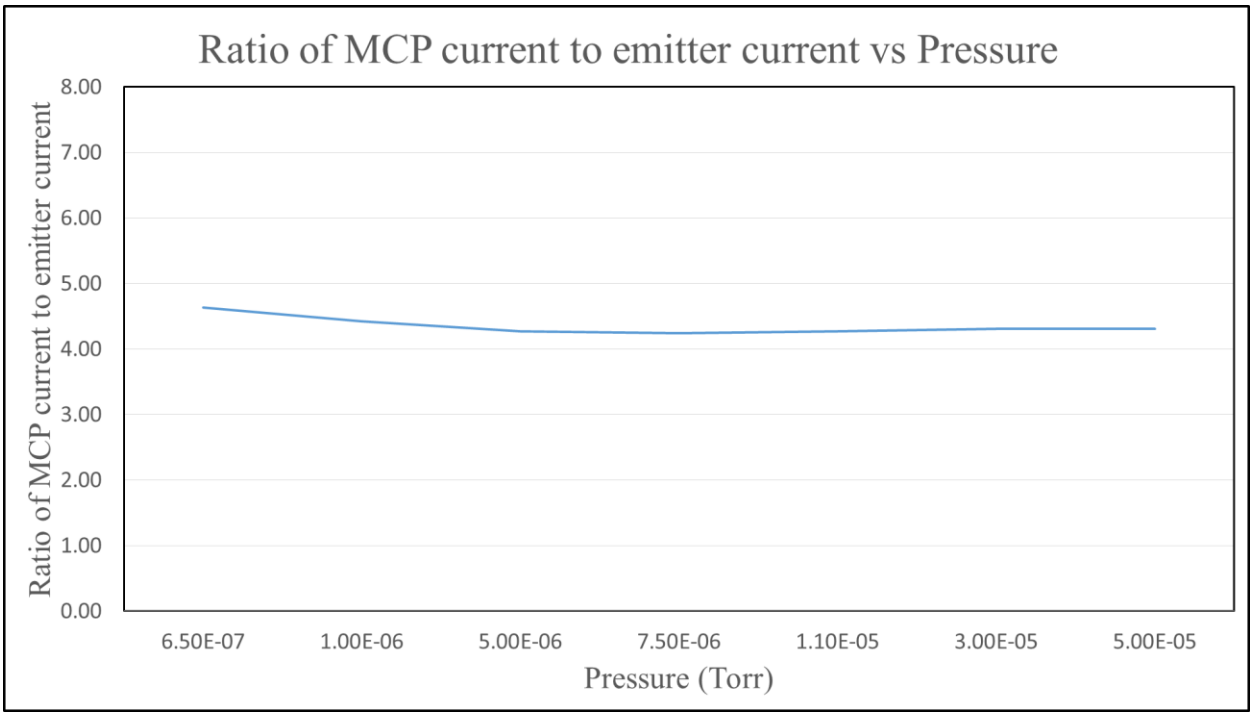

Figure 37: Ratio of MCP current to emitter current for different chamber pressures.

Chapter 6-Conclusions and Future Work

This thesis has detailed the electrical design of the first ram wind sensor for use in CubeSats. Through both bench testing and vacuum testing, the basic functionality of the REDD electronics was verified. The largest task to complete before this instrument can be used in flight is a full system calibration with an ion source after integrating with the complete mechanical assembly. The REDD sensor current measurement was calibrated through bench testing, but in order to meet the full requirements of all the current inputs a board re-layout needs to be done for the current measurement board. This board re-layout needs to incorporate a guard trace around the inverting input pin of the TIA in order to prevent external leakages from reaching the input, and also to take full advantage of the LMP7721's ultra-low input bias current. Furthermore, the through-hole feedback resistors of the TIA should be replaced with SMD resistors having large 1206 pads to reduce parasitic inductances and resistances at the inverting node junction. These measures would ensure that the TIA exhibits ideal I-V characteristics.

A new schematic and layout has been done to create the next-generation design of the current measurement board. Once this is fabricated and populated, additional testing must be done to validate the REDD design as a whole. A test plan for this is given below.

- Obtain LMP7721 evaluation board
- Obtain next-generation current measurement board
- Perform tests on bench to :
    1. Validate REDD's ability to measure low currents
    2. Calibrate current measurement board over the 100 pA to 10 μA range using a precision current source
- Install sensor and boards in vacuum chamber
- Test response of MCP versus pressure with emitter current constant
- Use draw-out grid to generate I-V curves
- Integrate REDD electronics with complete mechanical assembly and test prototype with ion source in lab
- Verify full REDD instrument functionality with neutral beam facility in the Naval Research Lab or at the NASA Marshall Launch Facility

References

[1]R. F. Woodman and C. La Hoz, J. Geophys. Res. **81,** 5447 (1976).

[2]B. G. Fejer, J. Atmos. Sol.-Terr. Phys. **59,** 1465 (1997).

[3]D. L. Hysell, J. Atmos. Sol.-Terr. Phys. **62,** 1037 (2000).

[4]W. B. Hanson, U. Ponzi, C. Arduini, and M. Di Ruscio, J. Astronaut. Sci. **40,** 429 (1992).

[5]G. D. Earle, J. H. Klenzing, P. A. Roddy, W. A. Macaulay, M. D. Perdue, and E. L. Patrick, Rev. Sci. Instrum. **78**, 114501 (2007).

[6]Moretto, Therese, *Space Weather, 6,* doi: 10.1029/2008SW000441, 2008.

[7]E. C. Whipple, Proc. IRE **47,** 2023 (1959).

[8]W.C. Knudsen, J. Geophys. Res. **71,** 4669 (1966).

[9]D. W. Marquardt, J. Soc. Ind. Appl. Math. **11,** 431 (1963).

Appendix A: Schematics

Main Board

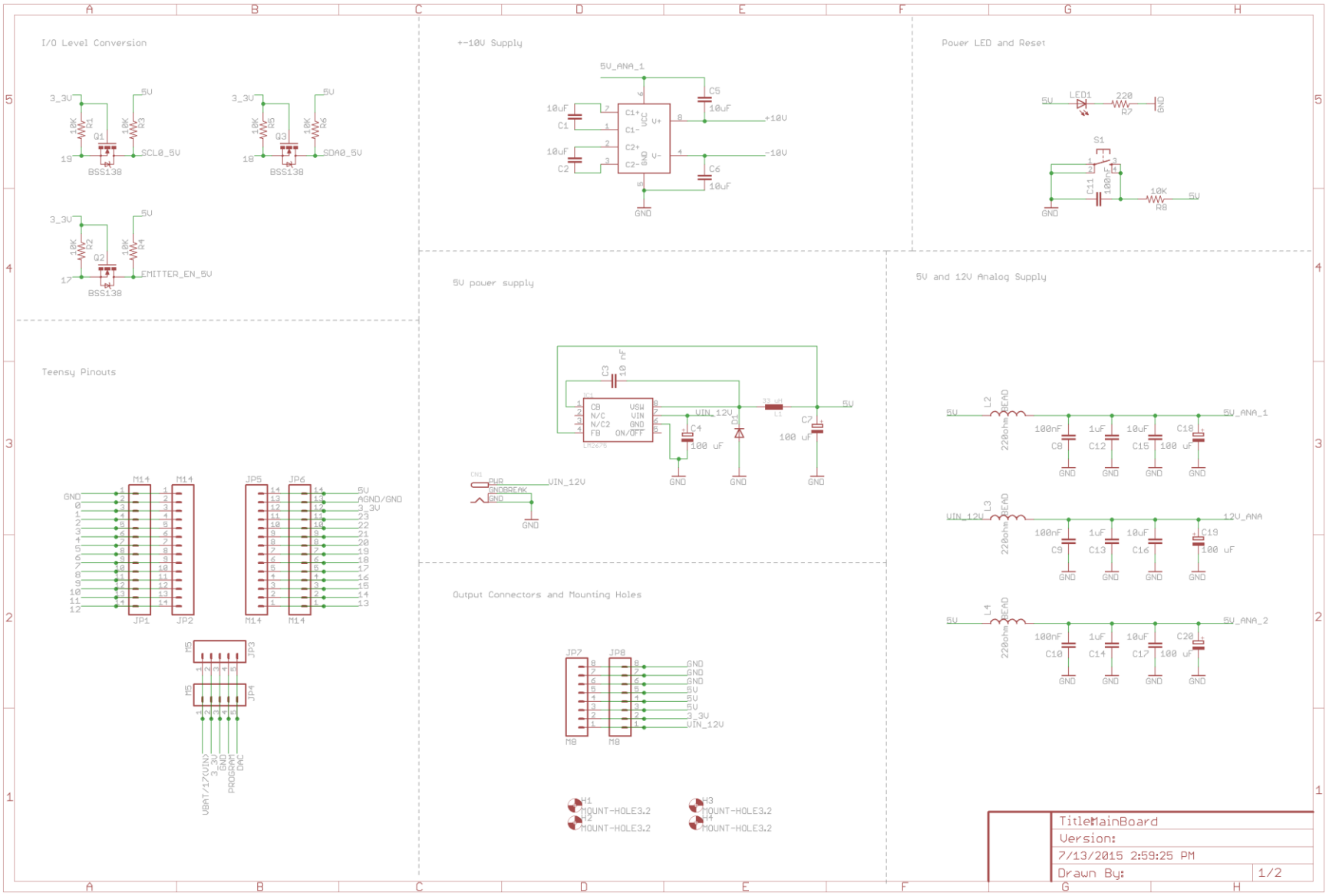
I/O Level Conversion
+-10V Supply
Power LED and Reset
5V power supply
5V and 12V Analog Supply
Teensy Pinouts
Output Connectors and Mounting Holes
BSS138
SCL0_5V
SDA0_5V
EMITTER_EN_5V
5V_ANA_1
+10V
-10V
VIN_12V
12V_ANA
5V_ANA_2
AGND/GND
MOUNT-HOLE3.2
Title:MainBoard
Version:
7/13/2015 2:59:25 PM
Drawn By:
1/2

Main Board

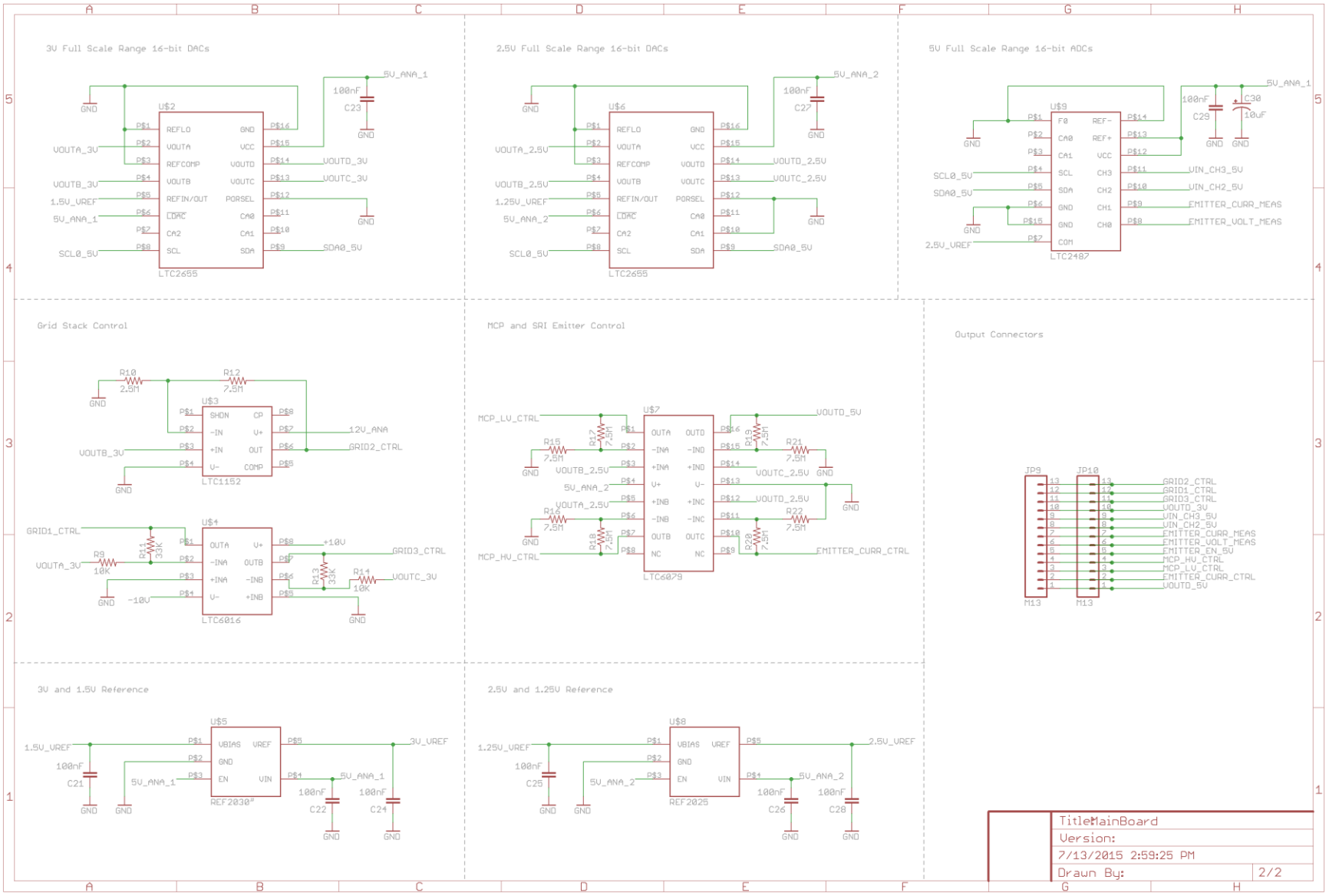
3V Full Scale Range 16-bit DACs
2.5V Full Scale Range 16-bit DACs
5V Full Scale Range 16-bit ADCs
Grid Stack Control
MCP and SRI Emitter Control
Output Connectors
3V and 1.5V Reference
2.5V and 1.25V Reference
LTC2655
LTC2655
LTC2487
LTC1152
LTC6016
LTC6079
REF2030
REF2025
JP9
JP10
M13
M13
Title:MainBoard
Version:
7/13/2015 2:59:25 PM
Drawn By:
2/2

High-Voltage Converter Board

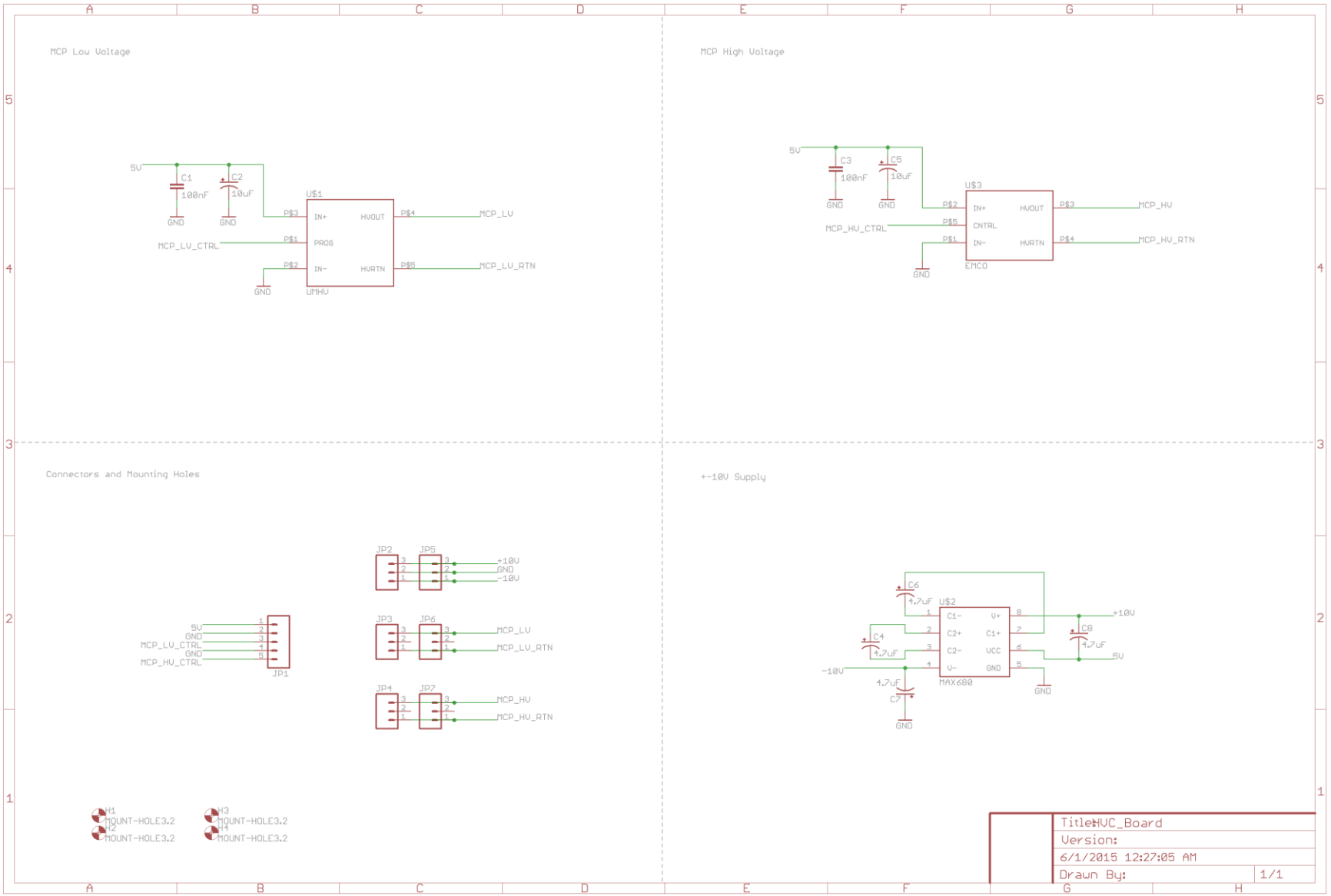

Current Measurement Board

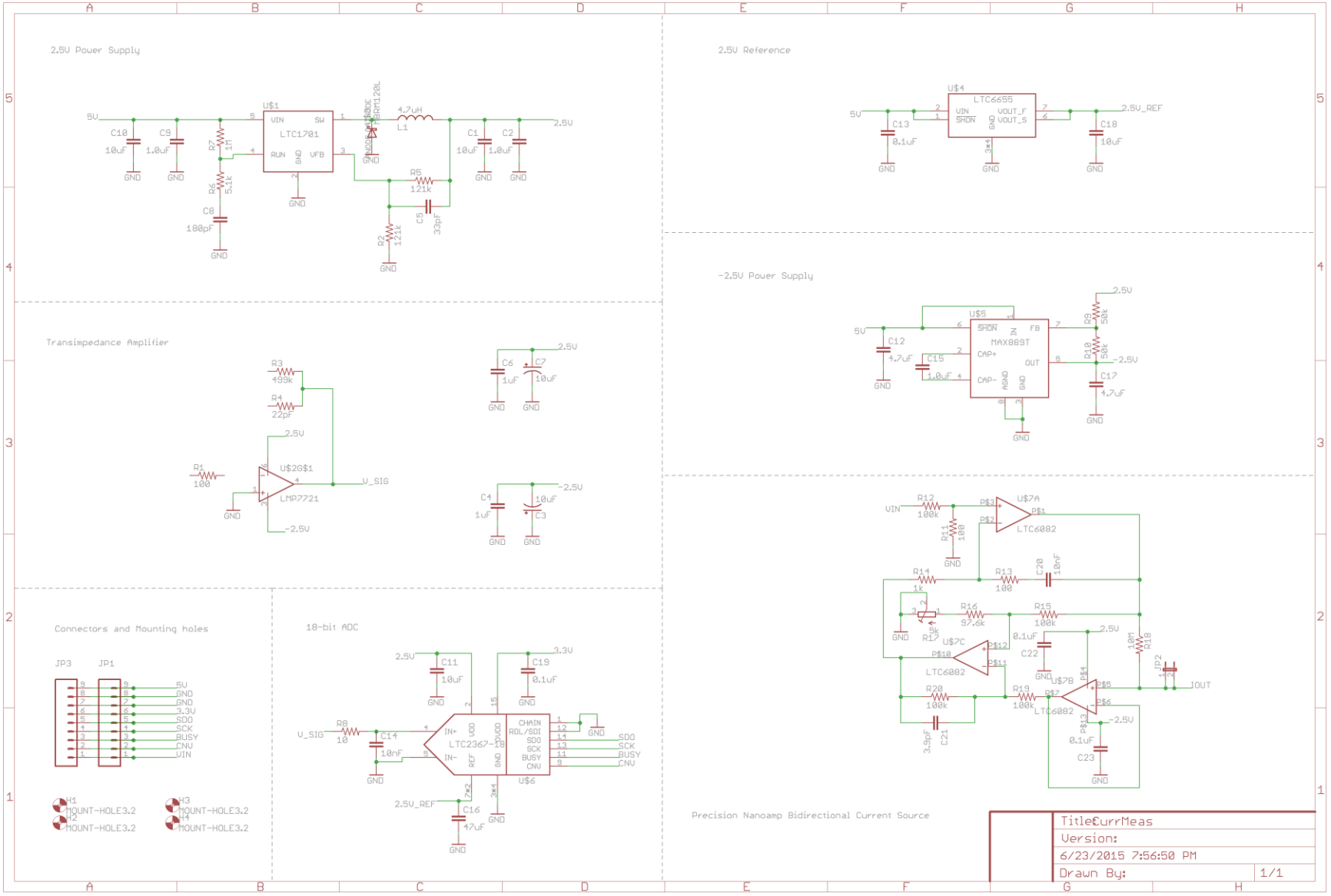

SRI Emitter Control Board

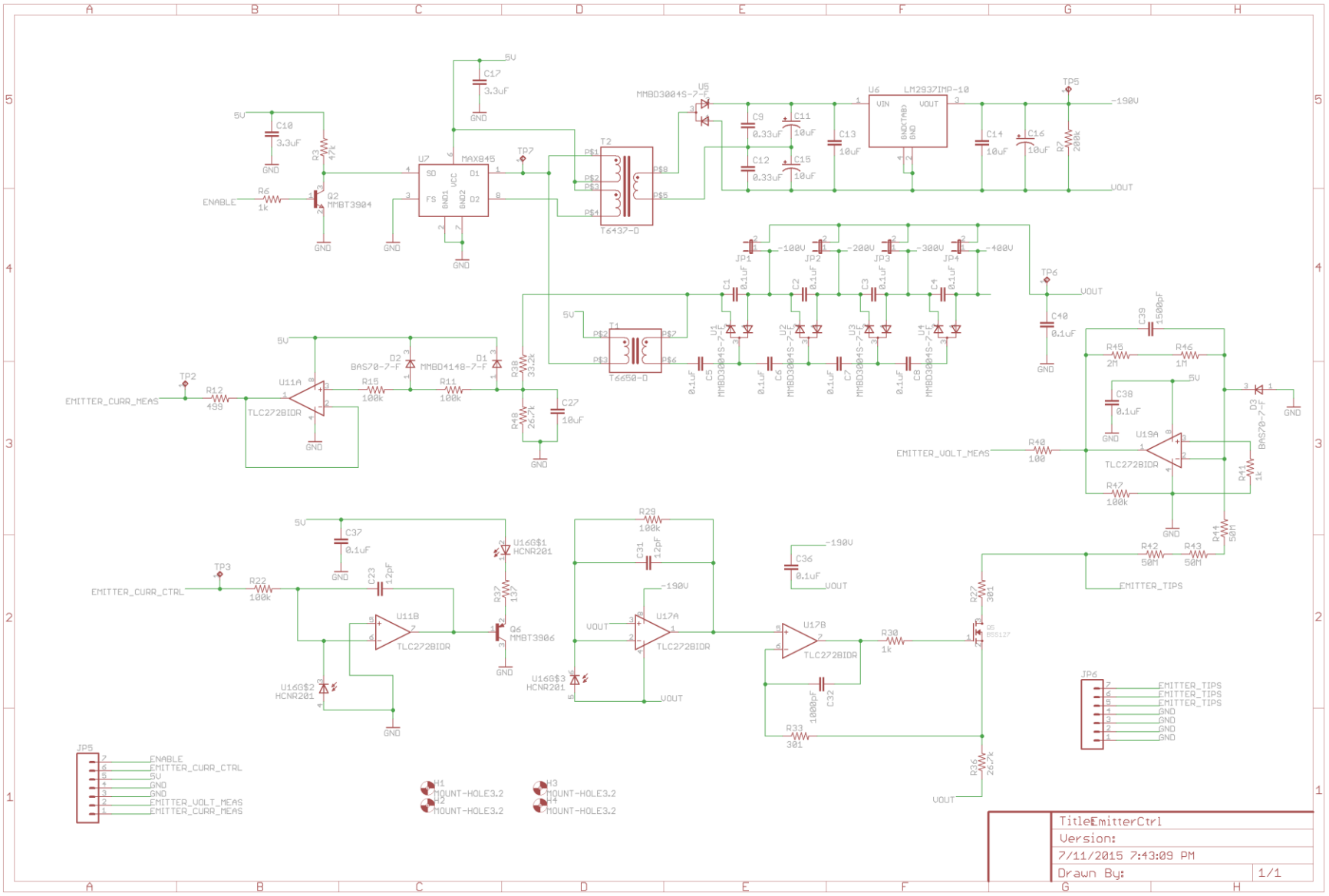

Appendix B: Board Layouts

Main Board

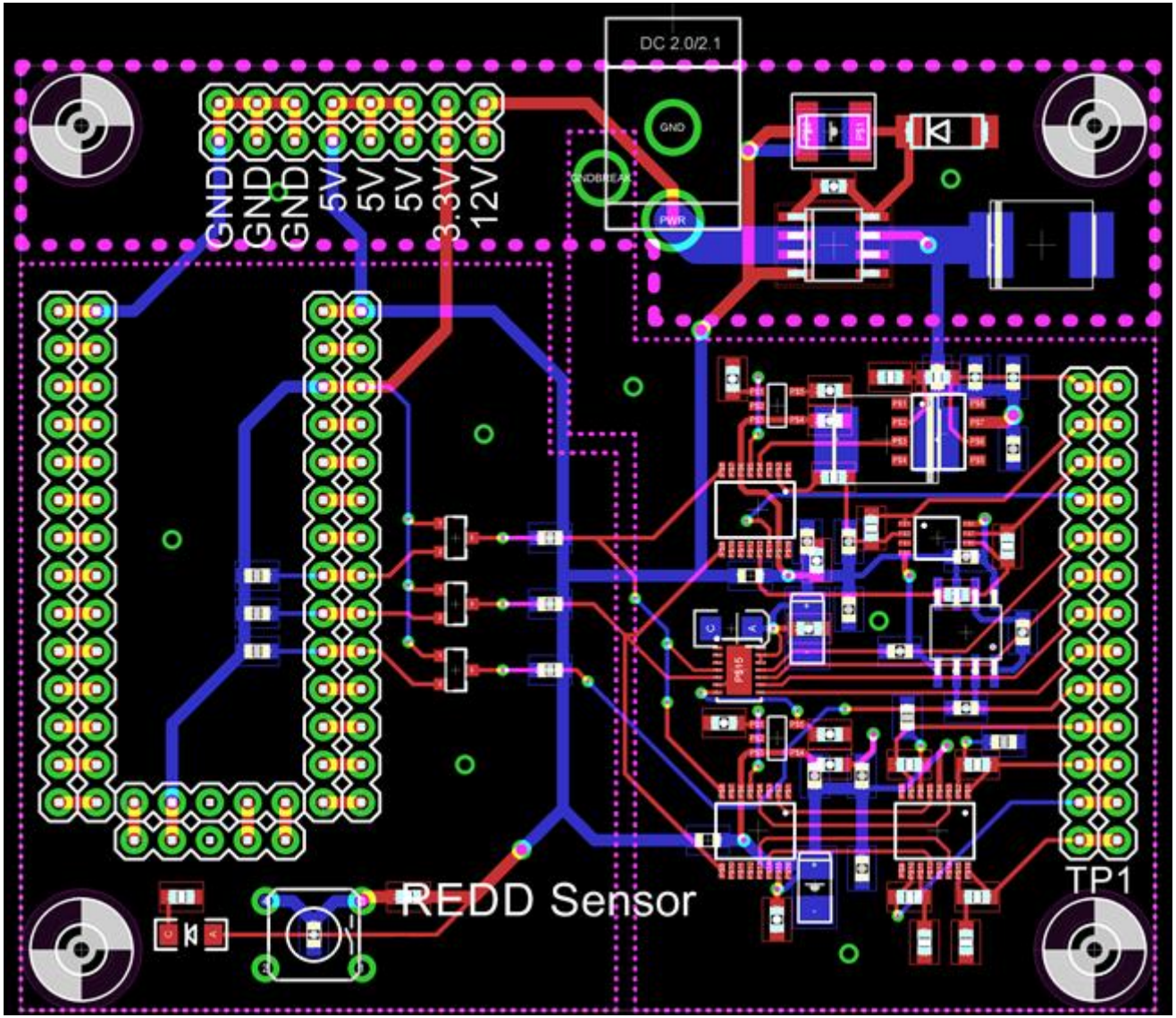

High-Voltage Converter Board

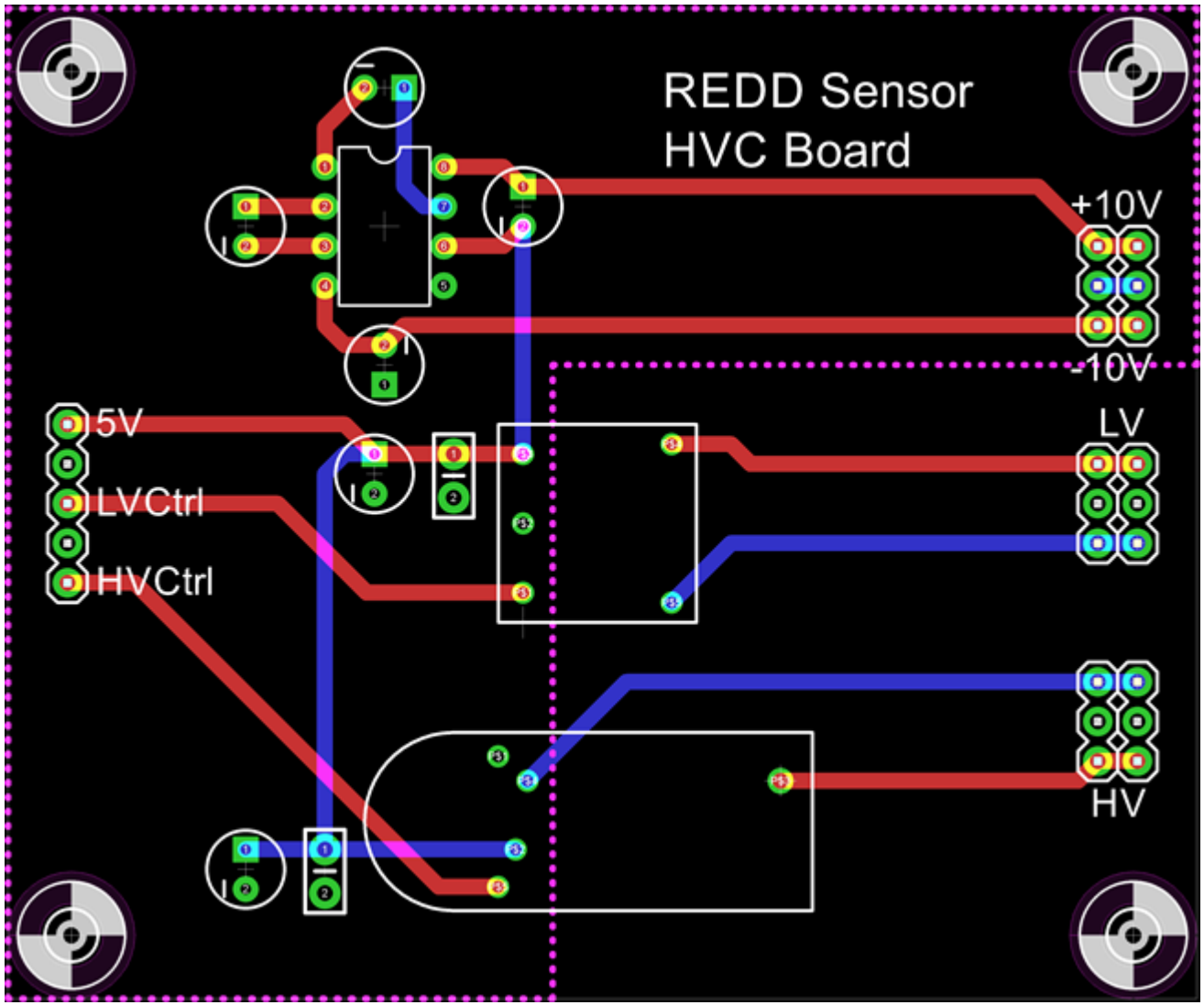

Current Measurement Board

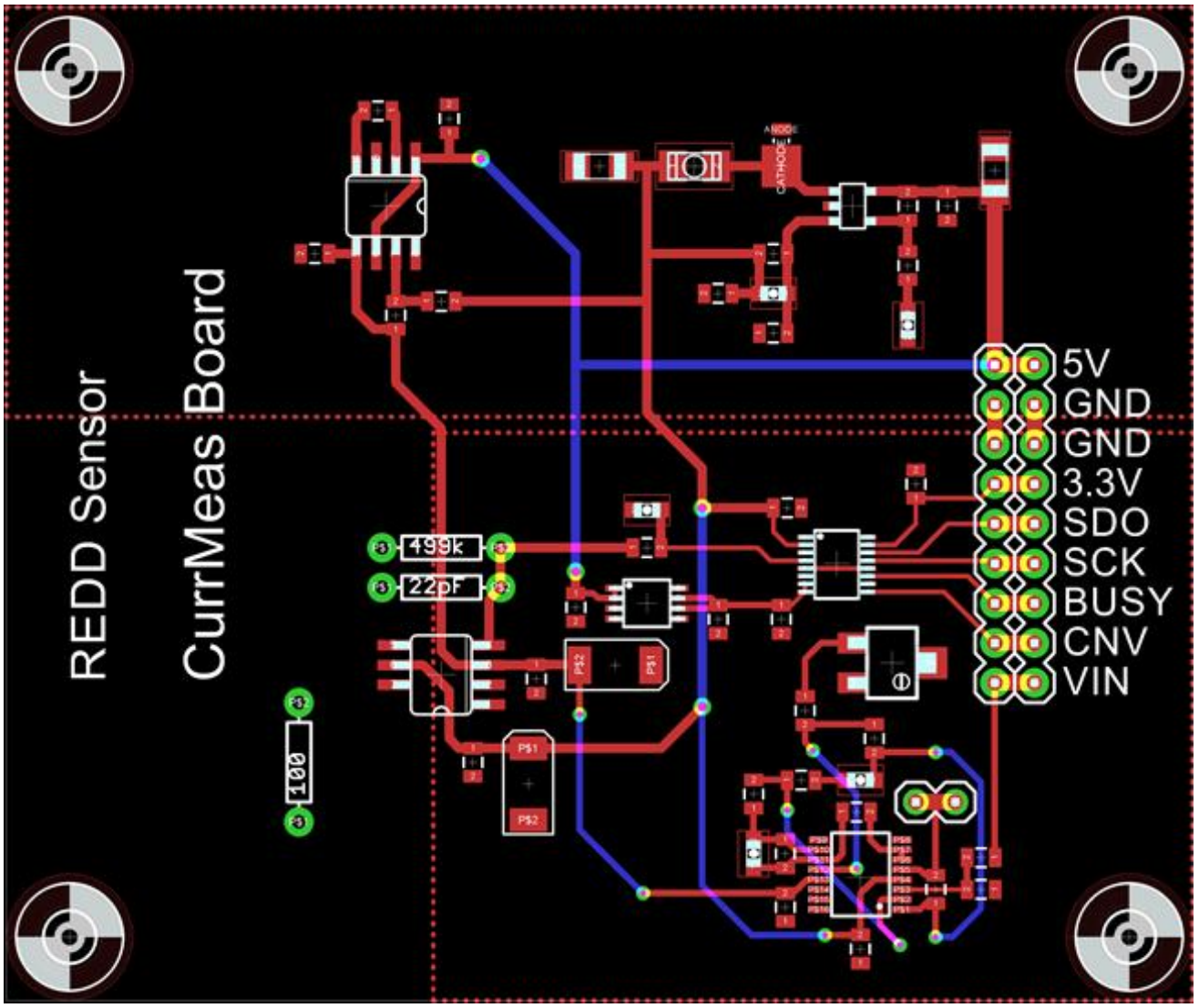

SRI Emitter Control Board

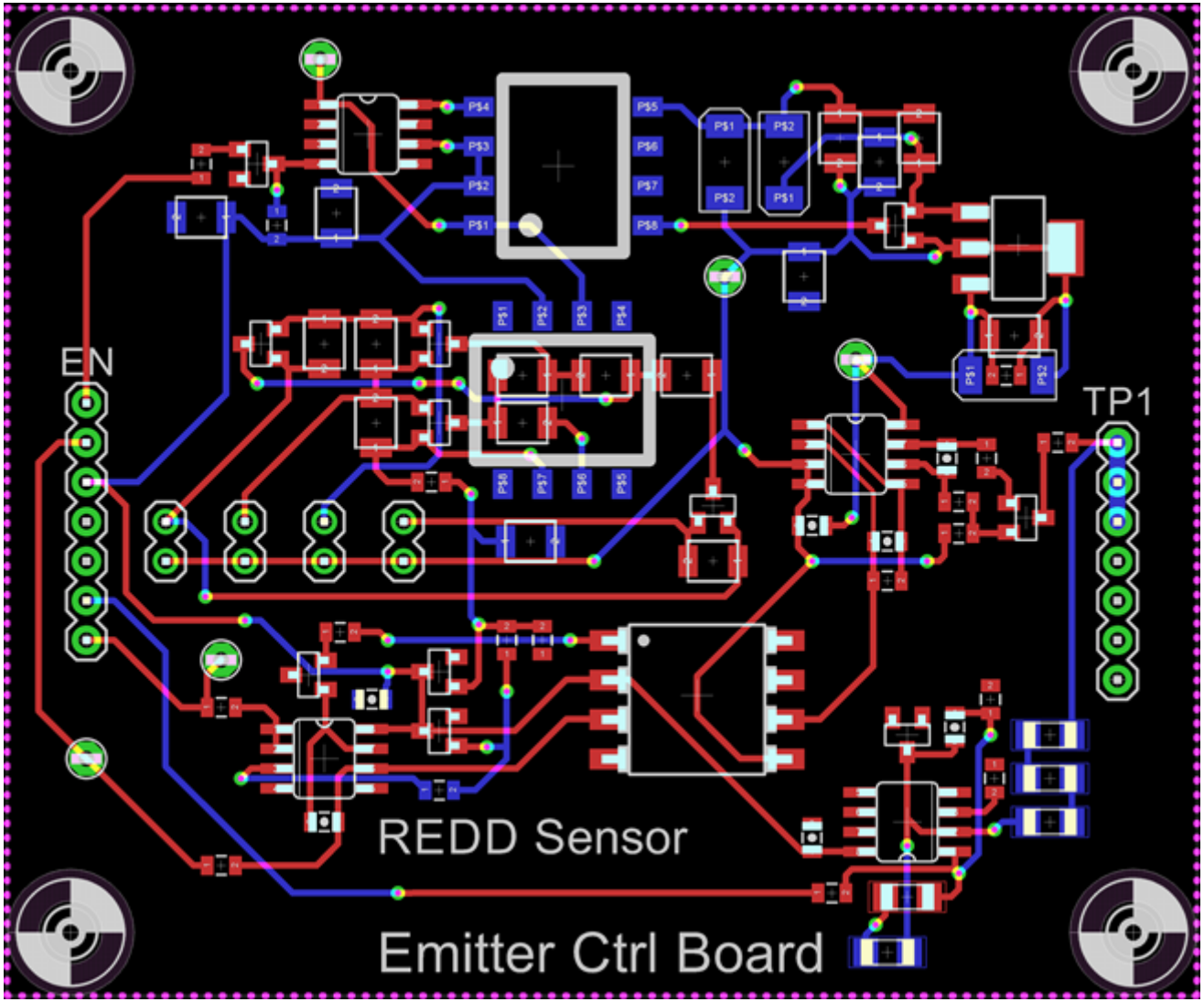

Appendix C: Parts Lists

Main Board

Item #	Qty	Ref Des	Manufacturer	Mfg Part #	Dist. Part #	Description	Package	Type
1	7	C1, C2, C5, C6, C15, C16, C17	Murata Electronics North America	GRM188R61E106MA73D	490-7202-1-ND	CAP CER 10UF 25V 20% X5R 0603	0603	smt
2	1	C3	Johanson Dielectrics Inc	500R14W103KV4T	709-1160-1-ND	CAP CER 10000PF 50V 10% X7R 0603	0603	smt
3	2	C4, C19	Vishay Sprague	594D107X0025R2T	718-1940-1-ND	CAP TANT 100UF 25V 20% 2824	2824	smt
4	3	C7, C18, C20	AVX Corporation	TPSB107M010R0400	478-5231-1-ND	CAP TANT 100UF 10V 20% 1210	1210	smt
5	13	C8, C9, C10, C11, C21, C22, C23, C24, C25, C26, C27, C28, C29	Samsung Electro-Mechanics America, Inc	CL10B104JA8NNNC	1276-1929-1-ND	CAP CER 0.1UF 25V 5% X7R 0603	0603	smt
6	3	C12, C13, C14	Murata Electronics North America	GRM188R61E105KA12D	490-3897-1-ND	CAP CER 1UF 25V 10% X5R 0603	0603	smt
7	1	C30	AVX Corporation	TPSA106K010R0900	478-1751-1-ND	CAP TANT 10UF 10V 10% 1206	1206	smt
8	1	CN1	CUI Inc	PJ-102AH	CP-102AH-ND	CONN PWR JACK 2.1X5.5MM HIGH CUR		thru-hole
9	1	D1	Diodes Incorporated	B120-13-F	B120-FDICT-ND	DIODE SCHOTTKY 20V 1A SMA	DO-214AC, SMA	smt
10	1	IC1	Texas Instruments	LM2675MX-5.0/NOPB	LM2675MX-5.0/NOPBCT-ND	IC REG BUCK 5V 1A 8SOIC	8SOIC	smt
11	1	L1	Taiyo Yuden	NR5040T330M	587-2370-1-ND	FIXED IND 33UH 1.2A 234 MOHM SMD	Nonstandard	smt
12	3	L2, L3, L4	Laird-Signal Integrity Products	LI0805G201R-10	240-2549-1-ND	FERRITE 700MA 250 OHMS 0805 SMD	0805	smt
13	1	LED1	Lite-On Inc	LTST-C150KRKT	160-1405-1-ND	LED SUPER RED CLEAR 1206 SMD	1206	smt
14	3	Q1, Q2, Q3	Fairchild Semiconductor	BSS138	BSS138CT-ND	MOSFET N-CH 50V 220MA SOT-23	SOT-23	smt
15	9	R1, R2, R3, R4, R5, R6, R8, R9, R14	Panasonic Electronic Components	ERJ-3EKF1002V	P10.0KHCT-ND	RES SMD 10K OHM 1% 1/10W 0603	0603	smt
16	1	R7	Panasonic Electronic Components	ERJ-3GEYJ221V	P220GCT-ND	RES SMD 220 OHM 5% 1/10W 0603	0603	smt
17	1	R10	Ohmite	HVC0603T2504FET	HVC0603T2504FETCT-ND	RES SMD 2.5M OHM 1% 1/10W 0603	0603	smt
18	2	R11, R13	Panasonic Electronic Components	ERJ-3EKF3302V	P33.0KHCT-ND	RES SMD 33K OHM 1% 1/10W 0603	0603	smt
19	9	R12, R15, R16, R17, R18, R19, R20, R21, R22	Rohm Semiconductor	KTR03EZPF7504	RHM7.5MAYCT-ND	RES SMD 7.5M OHM 1% 1/10W 0603	0603	smt
20	1	S1	Omron Electronics Inc-EMC Div	B3F-1005	SW793-ND	SWITCH TACTILE SPST-NO 0.05A 24V		thru-hole
21	1	U$1	Maxim Integrated	MAX680CSA+	MAX680CSA+-ND	IC REG MULTI CONFIG ADJ DL 8SOIC	8SOIC	smt
22	2	U$2, U$6	Linear Technology	LTC2655BIGN-L16#PBF	LTC2655BIGN-L16#PBF-ND	IC DAC 16BIT I2C/SRL 16SSOP	16SSOP	smt
23	1	U$3	Linear Technology	LTC1152IS8#PBF	LTC1152IS8#PBF-ND	IC OPAMP CHOPPER 700KHZ RRO 8SO	8SO	smt
24	1	U$4	Linear Technology	LT6016IMS8#PBF	LT6016IMS8#PBF-ND	IC OPAMP GP 3.3MHZ RRO 8MSOP	8MSOP	smt
25	1	U$5	Texas Instruments	REF2030AIDDCT	296-38496-1-ND	IC VREF SERIES 1.5V/3V 5SOT	5SOT	smt
26	1	U$7	Linear Technology	LTC6079IGN#PBF	LTC6079IGN#PBF-ND	IC OPAMP GP 750KHZ RRO 16SSOP	16SSOP	smt
27	1	U$8	Texas Instruments	REF2025AIDDCT	296-37989-1-ND	IC VREF SERIES 1.24V/2.5V 5SOT	5SOT	smt
28	1	U$9	Linear Technology	LTC2487IDE#PBF	LTC2487IDE#PBF-ND	IC ADC 16BIT DELTA SIG 14-DFN	14-DFN	smt

High-Voltage Converter Board

Item #	Qty	Ref Des	Manufacturer	Mfg Part #	Dist. Part #	Description	Package	Type
1	2	C1, C3	Kemet	C320C104J5R5TA	399-9775-ND	CAP CER 0.1UF 50V 5% RADIAL		thru-hole
2	2	C2, C5	Kemet	T350G106K035AT	399-3579-ND	CAP TANT 10UF 35V 10% RADIAL		thru-hole
3	4	C4, C6, C7, C8	Kemet	T350G475K050AT	399-3581-ND	CAP TANT 4.7UF 50V 10% RADIAL		thru-hole
4	1	U$2	Maxim Integrated	MAX680EPA+	MAX680EPA+-ND	IC REG MULTI CONFIG ADJ DL 8DIP		thru-hole

Current Measurement Board

Item #	Qty	Ref Des	Manufacturer	Mfg Part #	Dist. Part #	Description	Package	Type
1	1	U$5	Maxim Integrated	MAX889TESA+	MAX889TESA+-ND	IC REG SWTCHD CAP INV ADJ 8SOIC	8SOIC	smt
2	2	C12, C17	Murata Electronics North America	GRM21BR71E475KA73L	490-9962-1-ND	CAP CER 4.7UF 25V 10% X7R 0805	0805	smt
3	1	C15	Murata Electronics North America	GRM21BR71E105KA99L	490-6484-1-ND	CAP CER 1UF 25V 10% X7R 0805	0805	smt
4	2	R9, R10	Vishay Thin Film	PNM0805E5002BST5	PNM0805-50KBCT-ND	RES SMD 50K OHM 0.1% 1/5W 0805	0805	smt
5	1	U$4	Linear Technology	LTC6655CHMS8-2.5#PBF	LTC6655CHMS8-2.5#PBF-ND	IC VREF SERIES 2.5V 8MSOP	8MSOP	smt
6	2	C13, C19	Murata Electronics North America	GRM21BR71E104KA01L	490-1673-1-ND	CAP CER 0.1UF 25V 10% X7R 0805	0805	smt
7	2	C11, C18	Murata Electronics North America	GRM21BR71A106KE51L	490-3905-1-ND	CAP CER 10UF 10V 10% X7R 0805	0805	smt
8	1	U$3	Linear Technology	LTC1701BES5#TRMPBF	LTC1701BES5#TRMPBFCT-ND	IC REG BUCK ADJ 0.5A TSOT23-5	TSOT23-5	smt
9	2	C1, C10	Murata Electronics North America	GRM31CR61E106KA12L	490-3373-1-ND	CAP CER 10UF 25V 10% X5R 1206	1206	smt
11	1	R6	Yageo	RT0805BRD071ML	YAG1821CT-ND	RES SMD 1M OHM 0.1% 1/8W 0805	0805	smt
12	1	R7	Yageo	RT0805BRD075K1L	YAG1938CT-ND	RES SMD 5.1K OHM 0.1% 1/8W 0805	0805	smt
13	2	R2, R5	Panasonic Electronic Components	ERA-6AEB1213V	P121KDACT-ND	RES SMD 121K OHM 0.1% 1/8W 0805	0805	smt
14	1	C8	Murata Electronics North America	GRM1885C1H181JA01D	490-1433-1-ND	CAP CER 180PF 50V 5% NP0 0603	0603	smt
15	1	C5	Murata Electronics North America	GRM1885C1H330JA01D	490-1415-1-ND	CAP CER 33PF 50V 5% NP0 0603	0603	smt
16	1	L1	Murata Electronics North America	LQH32CN4R7M33L	490-6619-1-ND	FIXED IND 4.7UH 650MA 150 MOHM	1210 (3225 Metric)	smt
17	1	U$1	ON Semiconductor	MBRM120LT3G	MBRM120LT3GOSCT-ND	DIODE SCHOTTKY 20V 1A POWERMITE	DO-216AA	smt
18	1	U$6	Linear Technology	LTC2367HMS-18#PBF	LTC2367HMS-18#PBF-ND	IC ADC 18BIT 500K 1CH 16MSOP	16MSOP	smt
19	1	C16	Murata Electronics North America	GRM21BR61A476ME15L	490-9961-1-ND	CAP CER 47UF 10V 20% X5R 0805	0805	smt
20	1	C14	Murata Electronics North America	GRM1885C1H103JA01D	490-9666-1-ND	CAP CER 10000PF 50V 5% NP0 0603	0603	smt
	1	R8	Vishay Dale	TNPW080510R0BEEA	541-2055-1-ND	RES SMD 10 OHM 0.1% 1/8W 0805	0805	smt
21	1	U$2	Texas Instruments	LMP7721MA/NOPB	LMP7721MA/NOPB-ND	IC OPAMP GP 17MHZ RRO 8SOIC	8SOIC	smt
22	4	C2, C4, C6, C9	Murata Electronics North America	GRM216R61E105KA12D	490-1700-1-ND	CAP CER 1UF 25V 10% X5R 0805	0805	smt
23	2	C3, C7	Vishay Sprague	293D106X0025C2TE3	718-1044-1-ND	CAP TANT 10UF 25V 20% 2312	2312	smt
24	1	R1	Vishay Dale	PTF56100R00BYEB	PTF100CCT-ND	RES 100 OHM .1% 10 PPM 1/8W		thru-hole
25	1	R3	Yageo	HHV-25JR-52-500K	500KAACT-ND	RES 500K OHM 1/4W 5% AXIAL		thru-hole
26	1	R4	Kemet	C410C220J1G5TA7200	399-4461-1-ND	CAP CER 22PF 100V 5% AXIAL		thru-hole

SRI Emitter Control Board

C	Qty	Ref Des	Manufacturer	Mfg Part #	Distributor	Dist. Part #	Description	Package	Type
1	9	C1, C2, C3, C4, C5, C6, C7, C8, C40	Kemet	C1210C104KCRACTU	Digi-Key	399-6747-1-ND	CAP CER 0.1UF 500V 10% X7R 1210	1210	smt
2	2	C9, C12	AVX Corporation	12101C334KAZ2A	Digi-Key	478-3582-1-ND	CAP CER 0.33UF 100V 10% X7R 1210	1210	smt
3	2	C10, C17	Kemet	C1210C335K3PACTU	Digi-Key	399-3144-1-ND	CAP CER 3.3UF 25V 10% X5R 1210	1210	smt
4	3	C11, C15, C16	AVX Corporation	TRJC106K035R0600	Digi-Key	478-7582-1-ND	CAP TANT 10UF 35V 10% 2312	2312	smt
5	3	C13, C14, C27	Taiyo Yuden	UMK325BJ106KM-T	Digi-Key	587-2247-1-ND	CAP CER 10UF 50V 10% X5R 1210	1210	smt
6	2	C23, C31	Yageo	CC0805JRNPO9BN120	Digi-Key	311-1100-1-ND	CAP CER 12PF 50V 5% NPO 0805	0805	smt
7	1	C32	Kemet	C0805C102J5GACTU	Digi-Key	399-1136-1-ND	CAP CER 1000PF 50V 5% NP0 0805	0805	smt
8	3	C36, C37, C38	Kemet	C0805C104K3RACTU	Digi-Key	399-1168-1-ND	CAP CER 0.1UF 25V 10% X7R 0805	0805	smt
9	1	C39	Kemet	C0805C152J5GACTU	Digi-Key	399-8027-1-ND	CAP CER 1500PF 50V 5% NP0 0805	0805	smt
10	1	D1	Diodes Incorporated	MMBD4148-7-F	Digi-Key	MMBD4148-FDICT-ND	DIODE GEN PURP 75V 200MA SOT23-3	SOT23-3	smt
11	2	D2, D3	Diodes Incorporated	BAS70-7-F	Digi-Key	BAS70-FDICT-ND	DIODE SCHOTTKY 70V 70MA SOT23-3	SOT23-3	smt
12	1	Q2	Fairchild Semiconductor	MMBT3904	Mouser	512-MMBT3904	Bipolar Transistors - BJT SOT-23 NPN GEN PUR	SOT23-3	smt
13	1	Q5	Diodes Incorporated	BSS127S-7	Digi-Key	BSS127S-7DICT-ND	MOSFET N-CH 600V 0.05A SOT23	SOT23-3	smt
14	1	Q6	Fairchild Semiconductor	MMBT3906	Mouser	512-MMBT3906	Bipolar Transistors - BJT PNP General Purpose	SOT23-3	smt
15	1	R3	Panasonic Electronic Components	ERJ-6ENF4702V	Digi-Key	P47.0KCCT-ND	RES SMD 47K OHM 1% 1/8W 0805	0805	smt
16	1	R7	Panasonic Electronic Components	ERJ-6ENF2003V	Digi-Key	P200KCCT-ND	RES SMD 200K OHM 1% 1/8W 0805	0805	smt
17	5	R11, R15, R22, R29, R47	Panasonic Electronic Components	ERJ-6ENF1003V	Digi-Key	P100KCCT-ND	RES SMD 100K OHM 1% 1/8W 0805	0805	smt
18	1	R12	Panasonic Electronic Components	ERJ-6ENF4990V	Digi-Key	P499CCT-ND	RES SMD 499 OHM 1% 1/8W 0805	0805	smt
19	2	R27, R33	Panasonic Electronic Components	ERJ-6ENF3010V	Digi-Key	P301CCT-ND	RES SMD 301 OHM 1% 1/8W 0805	0805	smt
20	3	R6, R30, R41	Panasonic Electronic Components	ERJ-6ENF1001V	Digi-Key	P1.00KCCT-ND	RES SMD 1K OHM 1% 1/8W 0805	0805	smt
21	2	R36, R48	Panasonic Electronic Components	ERJ-6ENF2672V	Digi-Key	P26.7KCCT-ND	RES SMD 26.7K OHM 1% 1/8W 0805	0805	smt
22	1	R37	Panasonic Electronic Components	ERJ-6ENF1370V	Digi-Key	P137CCT-ND	RES SMD 137 OHM 1% 1/8W 0805	0805	smt
23	1	R38	Panasonic Electronic Components	ERJ-6ENF3322V	Digi-Key	P33.2KCCT-ND	RES SMD 33.2K OHM 1% 1/8W 0805	0805	smt
24	1	R40	Panasonic Electronic Components	ERJ-6ENF1000V	Digi-Key	P100CCT-ND	RES SMD 100 OHM 1% 1/8W 0805	0805	smt
25	3	R42, R43, R44	Vishay Dale	CRHV1206AF50M0FNE5	Digi-Key	CRHV50.0MACT-ND	RES SMD 50M OHM 1% 0.3W 1206	1206	smt
26	1	R45	Vishay Dale	CRCW12062M00FKEA	Digi-Key	541-2.00MFCT-ND	RES SMD 2M OHM 1% 1/4W 1206	1206	smt
27	1	R46	Vishay Dale	CRCW12061M00FKEAHP	Digi-Key	541-1.00MUCT-ND	RES SMD 1M OHM 1% 1/2W 1206	1206	smt
28	5	TP2, TP3, TP5, TP6, TP7	Keystone Electronics	5001	Digi-Key	534-5001	Circuit Board Hardware - PCB TEST POINT BLACK		thru-hole
29	1	T1	Coilcraft	T6650-D	**We will provide for assembly**	T6650-DLB	TRANSFORMER, MINIATURE, SMT, 1:5		smt
30	1	T2	Coilcraft	T6437-D	**We will provide for assembly**	T6437-DLB	TRANSFORMER, 1CT:1, SMT		smt
31	5	U1, U2, U3, U4, U5	Diodes Incorporated	MMBD3004S-7-F	Digi-Key	MMBD3004S-FDICT-ND	DIODE ARRAY GP 300V 225MA SOT23	SOT23-3	smt
32	1	U6	Texas Instruments	LM2937IMPX-10/NOPB	Digi-Key	LM2937IMPX-10/NOPBCT-ND	IC REG LDO 10V 0.4A SOT223	SOT223	smt
33	1	U7	Maxim Integrated	MAX845ESA+T	Digi-Key	MAX845ESA+TCT-ND	IC DRVR TRANSF ISO 8-SOIC	SOIC-8	smt
34	3	U11, U17, U19	Texas Instruments	TLC272BIDR	Mouser	595-TLC272BIDR	Operational Amplifiers - Op Amps LinCMOS Precision Dual Op Amp	SOIC-8	smt
35	1	U16	Avago Technologies US Inc.	HCNR201-300E	Digi-Key	516-1609-5-ND	OPTOISO 5KV LINEAR PHVOLT 8DIPGW	8DIPGW	smt

Appendix D: Assembled Electronics

Main Board

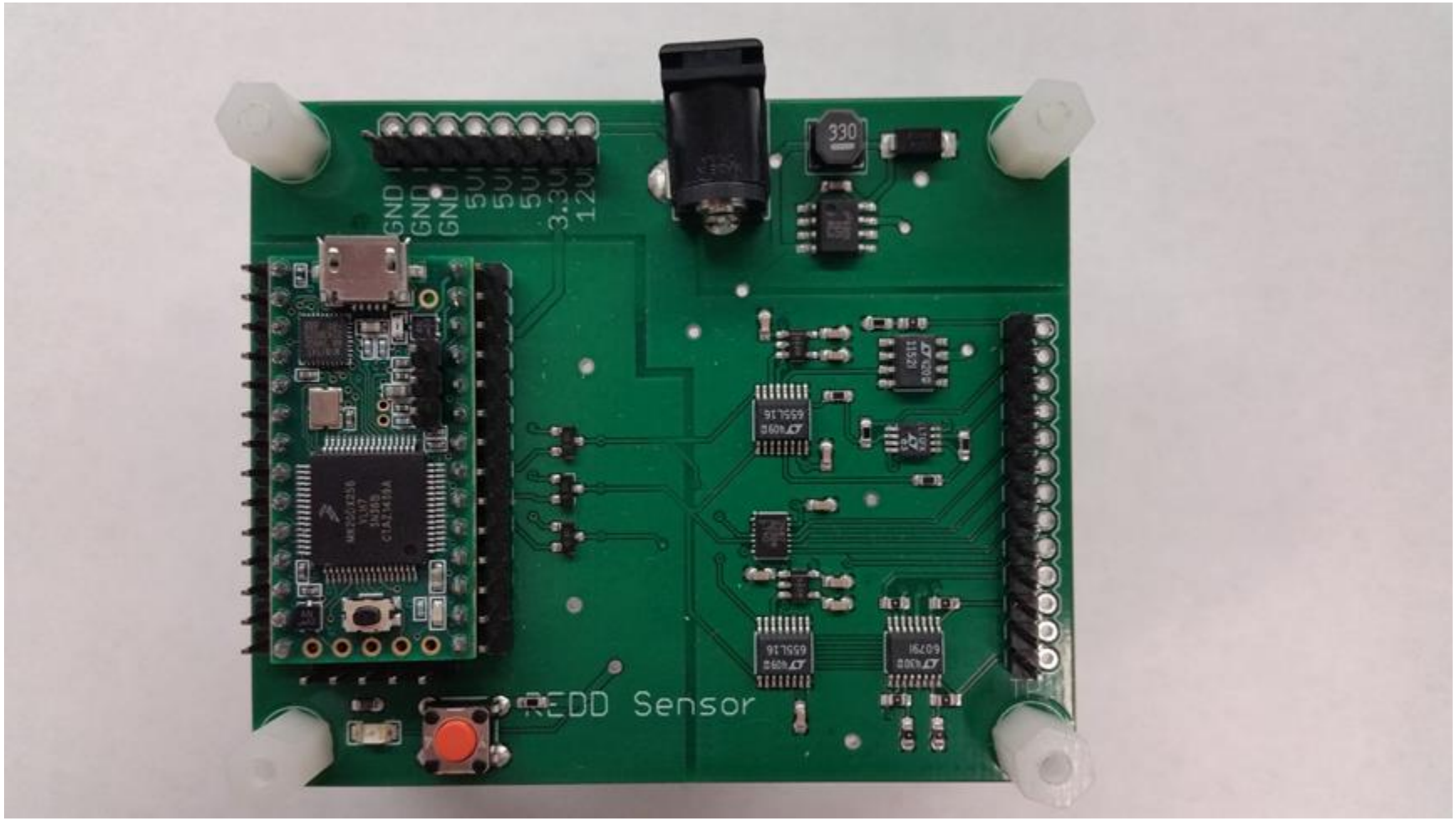

High-Voltage Converter Board

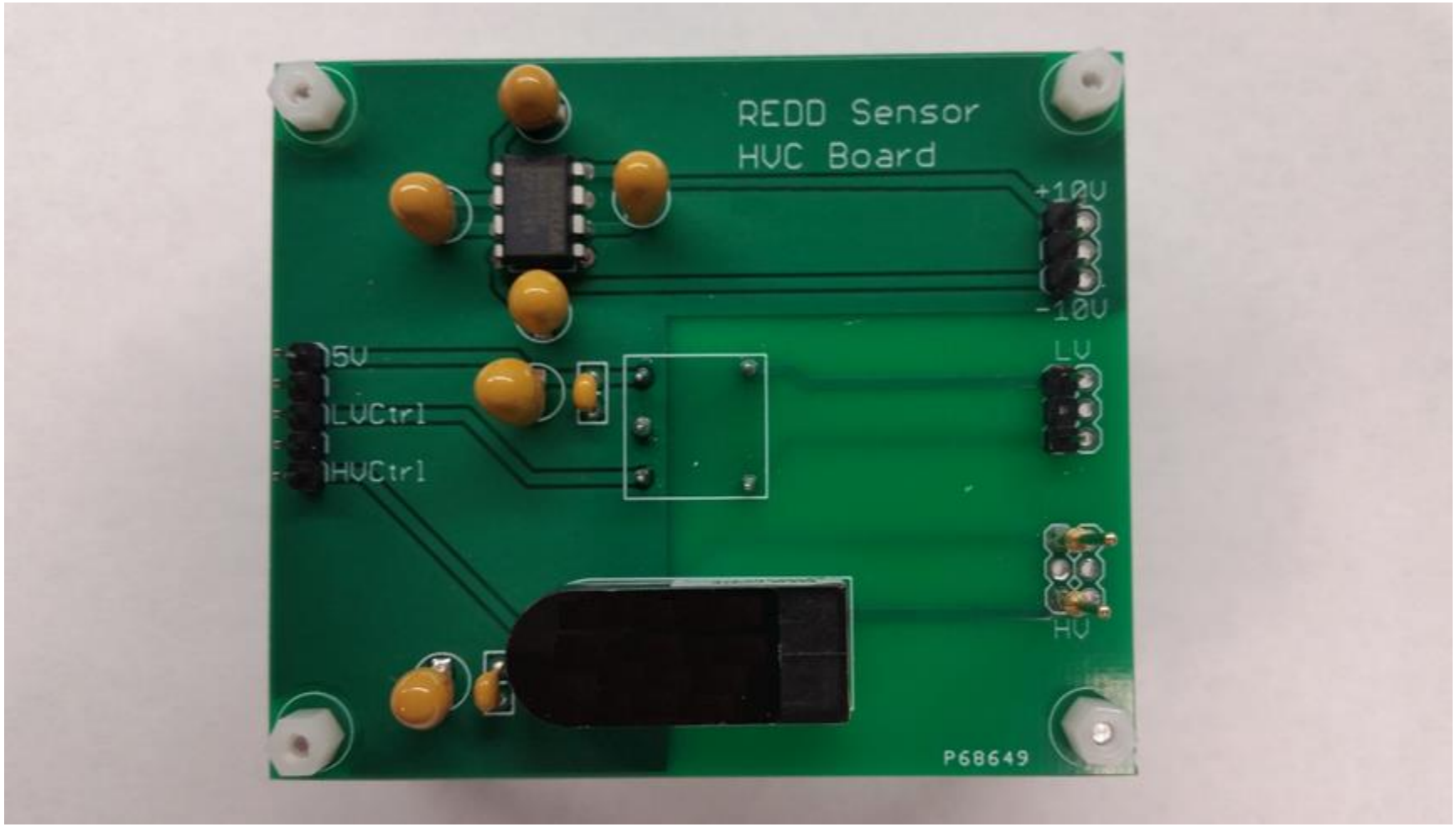

Current Measurement Board

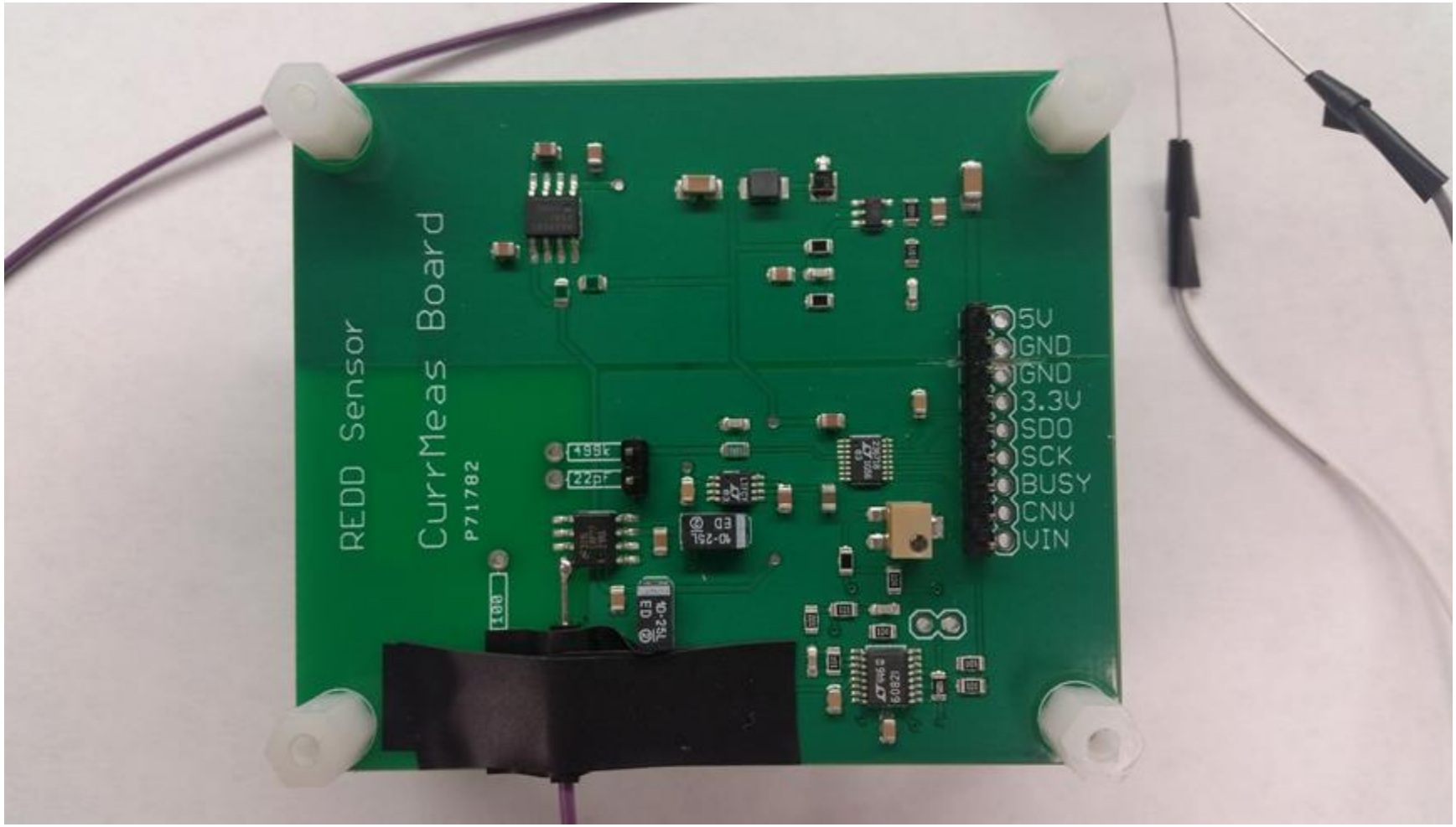

SRI Emitter Control Board

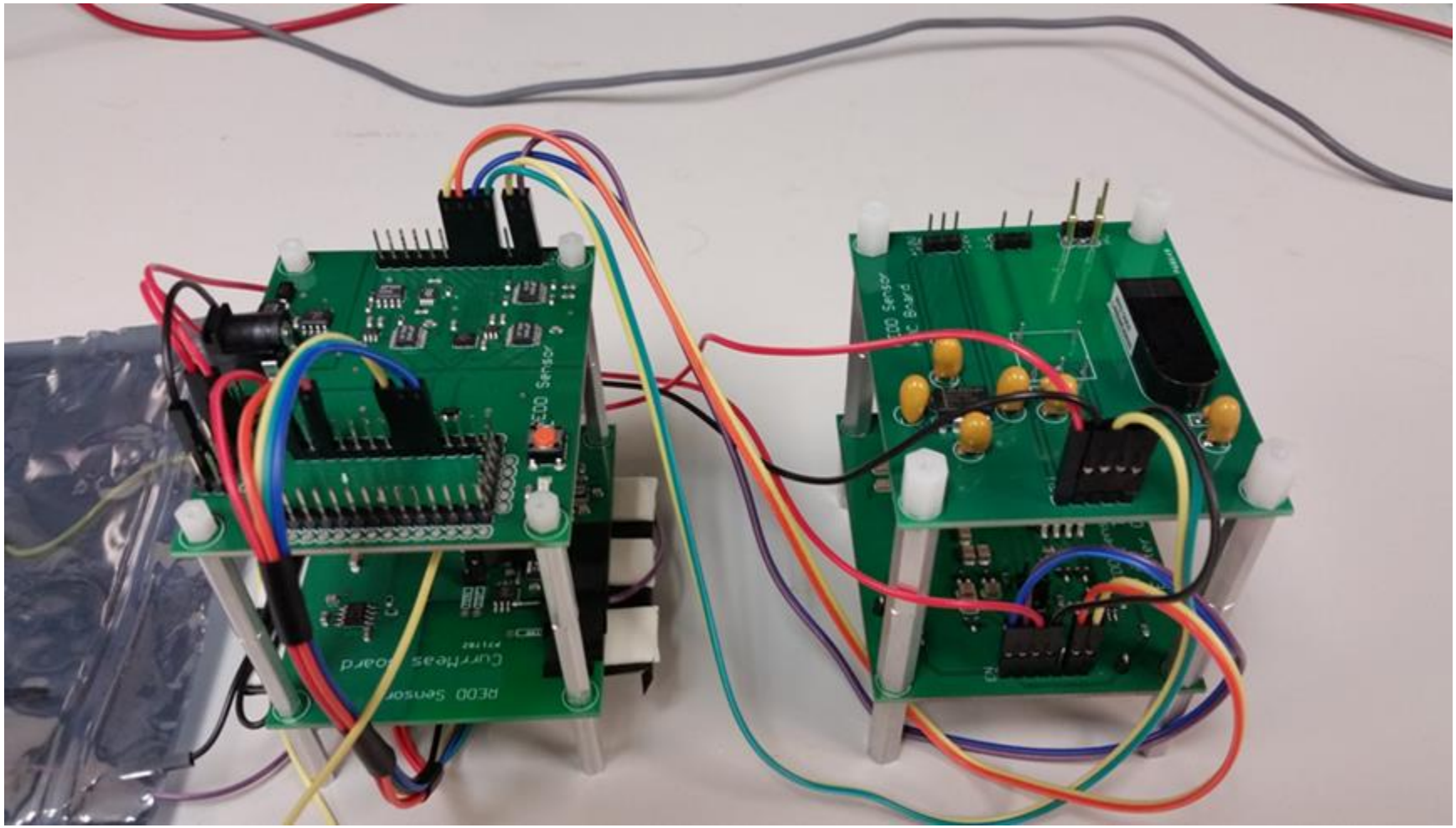

Appendix E: Wiring Diagrams

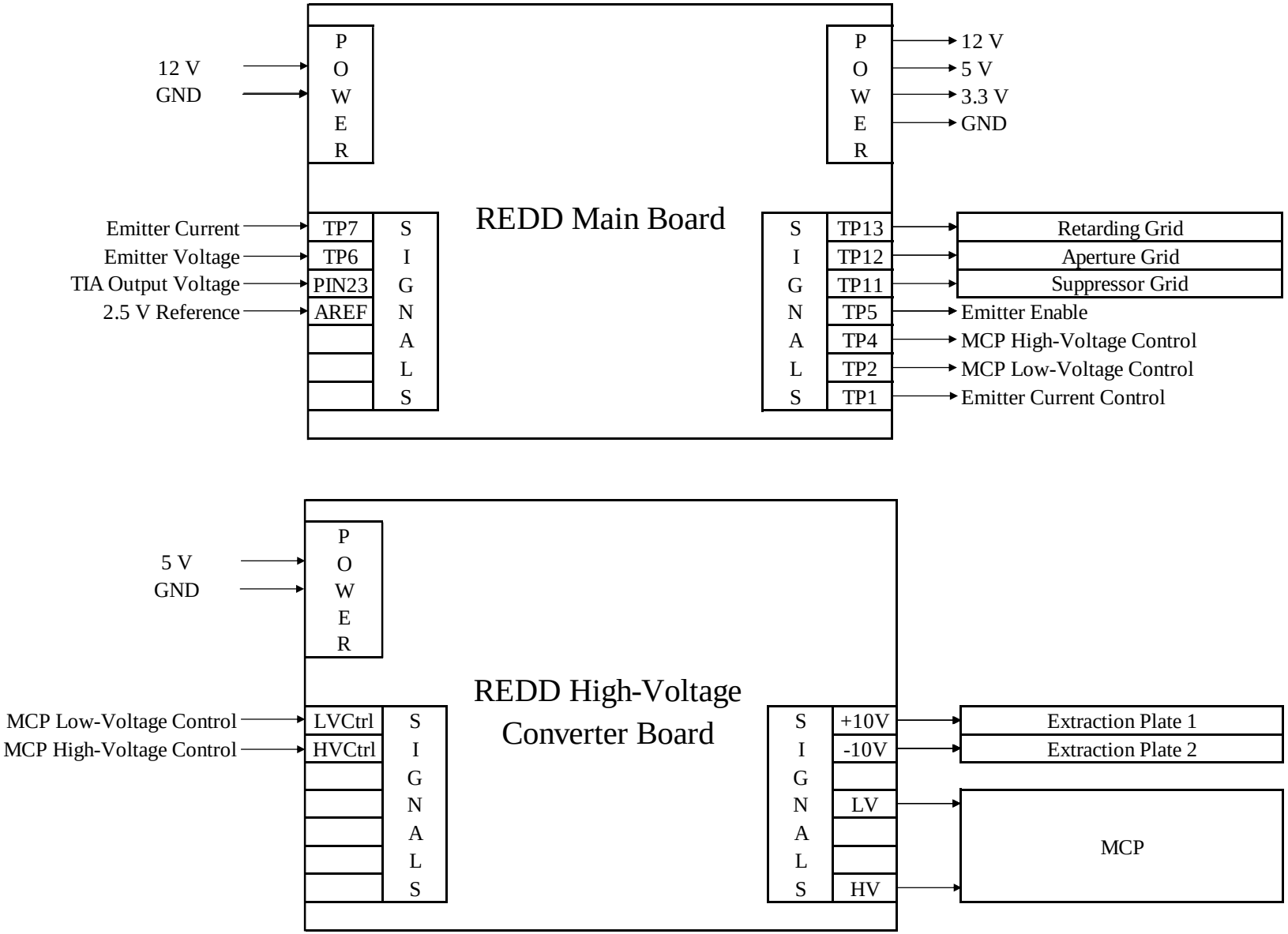
REDD Main Board
12 V
GND
POWER
Emitter Current
Emitter Voltage
TIA Output Voltage
2.5 V Reference
TP7
TP6
PIN23
AREF
SIGNALS
POWER
12 V
5 V
3.3 V
GND
SIGNALS
TP13
TP12
TP11
TP5
TP4
TP2
TP1
Retarding Grid
Aperture Grid
Suppressor Grid
Emitter Enable
MCP High-Voltage Control
MCP Low-Voltage Control
Emitter Current Control
REDD High-Voltage Converter Board
5 V
GND
POWER
MCP Low-Voltage Control
MCP High-Voltage Control
LVCtrl
HVCtrl
SIGNALS
SIGNALS
+10V
-10V
LV
HV
Extraction Plate 1
Extraction Plate 2
MCP

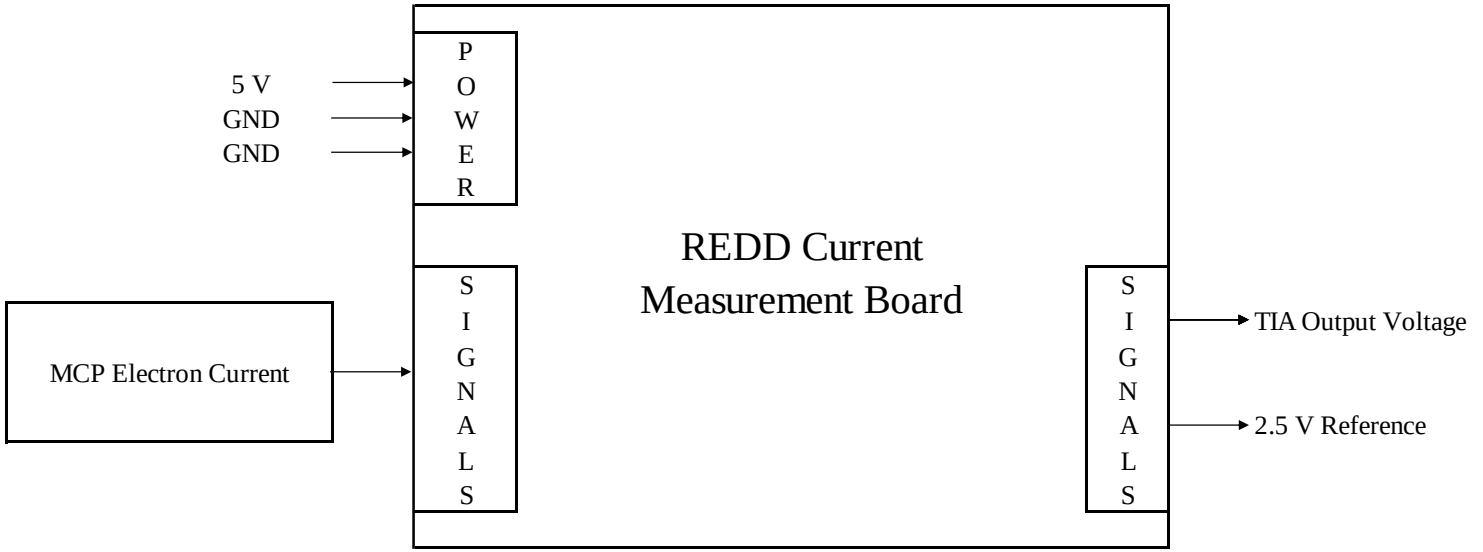
5 V
GND
GND
POWER
REDD Current
Measurement Board
SIGNALS
MCP Electron Current
SIGNALS
TIA Output Voltage
2.5 V Reference

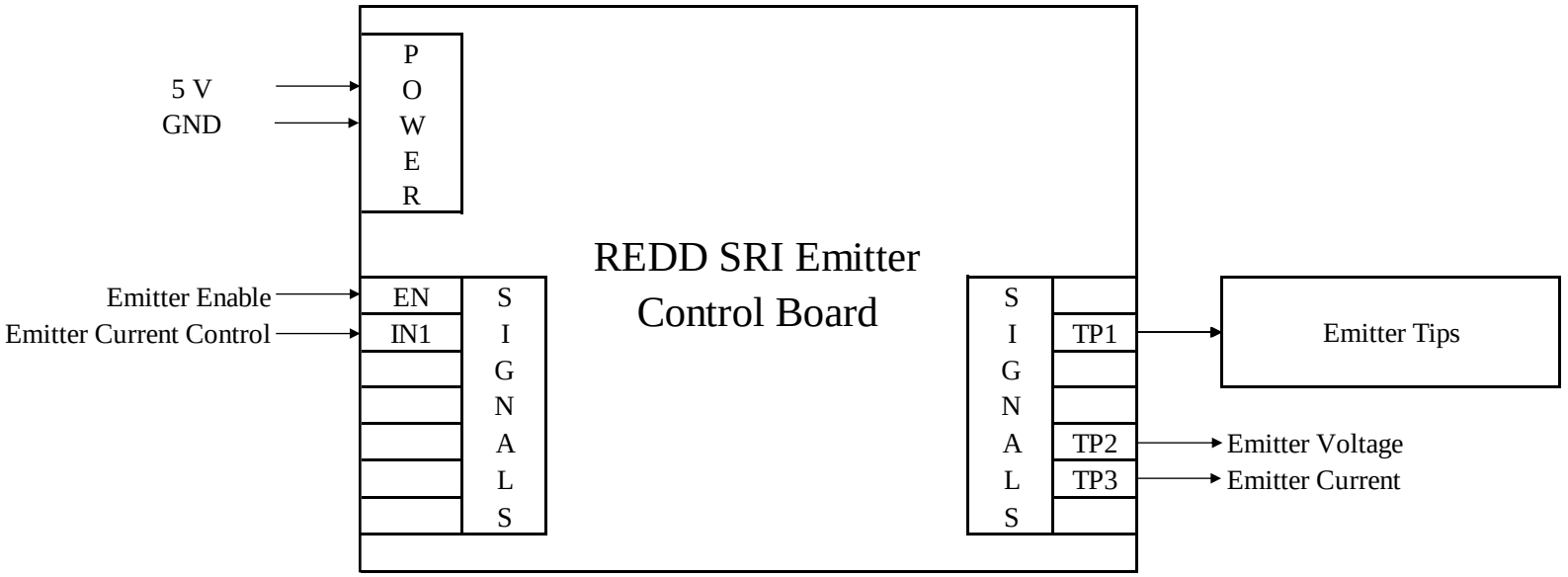
5 V
GND
POWER
REDD SRI Emitter
Control Board
Emitter Enable
Emitter Current Control
EN
IN1
SIGNALS
SIGNALS
TP1
TP2
TP3
Emitter Tips
Emitter Voltage
Emitter Current